Physics of Plasmas

On the axisymmetric stability of tokamaks with ferromagnetic walls

Cite as: Phys. Plasmas **27**, 102508 (2020); https://doi.org/10.1063/5.0018747
Submitted: 17 June 2020 . Accepted: 10 September 2020 . Published Online: 12 October 2020

O. P. Bardsley, and T. C. Hender

View Online Export Citation CrossMark

ARTICLES YOU MAY BE INTERESTED IN

MHD-blob correlations in NSTX
Physics of Plasmas **27**, 052505 (2020); https://doi.org/10.1063/5.0006515

Comment on "Resistive wall modes and related sideways forces in tokamak" [Phys. Plasmas 27, 012508 (2020)]
Physics of Plasmas **27**, 054701 (2020); https://doi.org/10.1063/5.0004705

Toroidal modeling of anisotropic thermal transport and energetic particle effects on stability of resistive plasma resistive wall mode
Physics of Plasmas **27**, 072502 (2020); https://doi.org/10.1063/5.0007426

NEW!
Sign up for topic alerts
New articles delivered to your inbox
AIP Publishing

© 2020 Author(s).

Physics of Plasmas ARTICLE scitation.org/journal/php

On the axisymmetric stability of tokamaks with ferromagnetic walls

Cite as: Phys. Plasmas **27**, 102508 (2020); doi: 10.1063/5.0018747
Submitted: 17 June 2020 · Accepted: 10 September 2020 ·
Published Online: 12 October 2020

View Online Export Citation CrossMark

O. P. Bardsley[a] and T. C. Hender

AFFILIATIONS

United Kingdom Atomic Energy Authority, Culham Centre for Fusion Energy, Culham Science Centre, Abingdon, Oxon OX14 3DB, United Kingdom

[a]Author to whom correspondence should be addressed: oliver.bardsley@ukaea.uk

ABSTRACT

Reduced activation ferritic steels are an attractive option for use in large structural components surrounding tokamak plasmas in future fusion power plants, but their ferromagnetic response to the confining magnetic fields must be properly understood. Simultaneously, the advantages of operating at high plasma elongation push tokamak designs toward scenarios that are more vulnerable to vertical displacement events. Passive conducting structures in present tokamaks slow these instabilities such that they may be feedback controlled, but the efficacy of this process is likely to be eroded by ferromagnetic effects. We approach two related analytical models—in cylindrical and spherical geometries—which qualitatively and quantitatively assess the impact of a ferritic steel wall on the vertical instability growth rate for a plasma of certain elongation. Distinct limits for magnetically thick and thin walls give key physical insight, but the dependence on magnetic permeability and wall geometry is, in general, quite complex. Equilibrium considerations, particularly with respect to radial force balance, are also encountered.

© *2020 Author(s). All article content, except where otherwise noted, is licensed under a Creative Commons Attribution (CC BY) license (http://creativecommons.org/licenses/by/4.0/).* https://doi.org/10.1063/5.0018747

I. INTRODUCTION

The first generation of nuclear fusion power plants will have to be built from materials capable of operating reliably when subjected to high fluences of 14 MeV neutrons. In particular, structural steels surrounding a burning tokamak plasma must be robust to both displacement damage and radioactivation in order to achieve sufficient operational availability and simplify the decommissioning process.[1] At present, the leading candidate materials for applications in the first wall and tritium breeding modules are reduced activation ferritic-martensitic (RAFM) steels[2,3] such as EUROFER-97;[4] unlike the stainless steels widely used in current tokamak experiments, these are ferromagnetic and as such have an effect on the confining magnetic field, which is more complex than just the electromagnetic induction of eddy currents. Ferromagnetism will alter both the equilibrium arrangement of flux surfaces—and in fact is used as a means of reducing toroidal field ripple[5,6]—and the time-dependent response of the vessel to changes in the plasma position or current.

At the same time, it is known to be advantageous for tokamak performance to operate at large values of plasma elongation, defined as the ratio of vertical to horizontal extents of its cross section.[7] Increasing elongation beyond the value it would naturally take in a uniform vertical field leads to axisymmetric instability; such vertical displacement events (VDEs), which would proceed at the Alfvén velocity in the absence of a vessel, are slowed to "resistive wall" timescales by the presence of surrounding conductors, to such a point they may be tamed by an active feedback control system.

Vertical stability is an important issue in tokamak reactor design; reliable plasma positioning is important for moderating divertor heat loads,[8] but at worst, VDEs involving high-energy plasmas can lead to extreme heat loads and electromagnetic forces upon the impact with the vessel wall, which will be intolerable in reactor-scale tokamaks.[9] Hence, there is a vital need to understand changes to the plasma's vertical stability characteristics when significant quantities of the material surrounding the plasma are exchanged for a ferromagnetic equivalent. It is this need that motivates the present study, which encompasses two closely related analytical model problems—one in an infinite aspect ratio (i.e., cylindrical) geometry (Sec. II) and one in a spherical geometry (Sec. III). We bookend these with a short introduction to ferromagnetism in tokamaks (Sec. I A) and a discussion of possible implications for the design of future devices with opportunities for further study (Sec. IV).

© Author(s) 2020

A. Ferromagnetic materials in tokamaks

Ferromagnetic materials are distinguished by a constitutive relation between the magnetic field $\boldsymbol{H}$ and magnetic flux density $\boldsymbol{B}$ within their volume, which differs dramatically from that for conventional materials, $\boldsymbol{B} = \mu_0 \boldsymbol{H}$, where μ_0 is the magnetic permeability of free space. The permeability of a ferromagnet is much larger at small $\boldsymbol{H}$ but saturates at large applied fields; in a tokamak, the dominant toroidal field can be expected to drive the material deep into saturation (the saturating magnetic field is $\mu_0 H_s \sim 0.25\,\mathrm{T}$ for EUROFER-97[4]). The effective magnetic permeability as experienced by the poloidal magnetic field, μ_1, then, depends upon the saturation magnetization of the material M_s and the applied toroidal magnetic field H_ϕ,

$$\frac{\mu_1}{\mu_0} \equiv \tilde{\mu} \approx 1 + \frac{M_s}{H_\phi}, \tag{1}$$

if the poloidal field strength is significantly weaker than the toroidal. This expression defines the *effective relative magnetic permeability* $\tilde{\mu}$; for EUROFER-97, the saturation magnetization is $\mu_0 M_s \sim 1.8\,\mathrm{T}$,[4] so a toroidal field of a couple of Tesla amounts to $\tilde{\mu} \sim 2$, with larger values for weaker fields.

Note that the boundary conditions across an interface between a vacuum and a ferromagnetic wall depend on the effective magnetic permeability of the material in question; in particular, both normal magnetic *flux* and tangential magnetic *field* must be conserved as follows:[10]

$$\langle \boldsymbol{B} \cdot \boldsymbol{n} \rangle = \left\langle \frac{\boldsymbol{B} \times \boldsymbol{n}}{\mu} \right\rangle = 0, \tag{2}$$

where $\boldsymbol{n}$ is the normal to the interface, μ ($=\mu_0$ or μ_1) is the effective magnetic permeability in each domain, and the angled brackets represent the jump across the boundary.

II. LARGE ASPECT RATIO TOKAMAKS: A CYLINDRICAL MODEL PROBLEM

We first consider a model problem in the large aspect ratio cylindrical limit, which is a particular case of previous work into ferromagnetic resistive wall modes (FRWMs).[11] Despite this, we detail the derivation here because (a) the dependence on $\tilde{\mu}$ for "slow" instabilities requires a different interpretation when large quantities of ferromagnetic material are present, (b) we are able to extract certain terms particular to this problem, which reveal the underlying physics, and (c) it will provide a useful primer for the more mathematically involved problem of Sec. III.

The layout is sketched in Fig. 1; the ferromagnetic, conducting wall is taken to be a continuous cylindrical shell of internal radius r_i and external radius r_e. It has an electrical conductivity σ and permeability μ_1, both of which are taken to be constant throughout its volume. The rest of the domain is vacuum with magnetic permeability μ_0. Polar co-ordinates (r, θ), as indicated in Fig. 1, are the natural choice in this geometry, and all quantities are assumed to be independent of the distance along the cylinder. The plasma is represented by a thin wire (we hereafter refer to this wire as "the plasma" despite making this rigid approximation), carrying a constant current I_p directed into the page, and located a small distance z_p above the origin; in equilibrium, the plasma height will be zero, but during a VDE, it will grow exponentially in time. A pair of divertor coils are represented by thin wires placed exterior to the wall at $r = r_c$, directly above and below the plasma at $\theta = [0, \pi]$, which each carry a constant current I_c in the same direction as the plasma current. Increasing the divertor current I_c relative to the plasma current I_p will increase the vertically destabilizing force on the plasma, thereby increasing the instability growth rate. Note that, in this infinite aspect ratio case, no vertical field need be applied in order to maintain the horizontal force balance. This geometry has been used previously for the study of the non-linear evolution of (non-ferromagnetic) VDEs.[12]

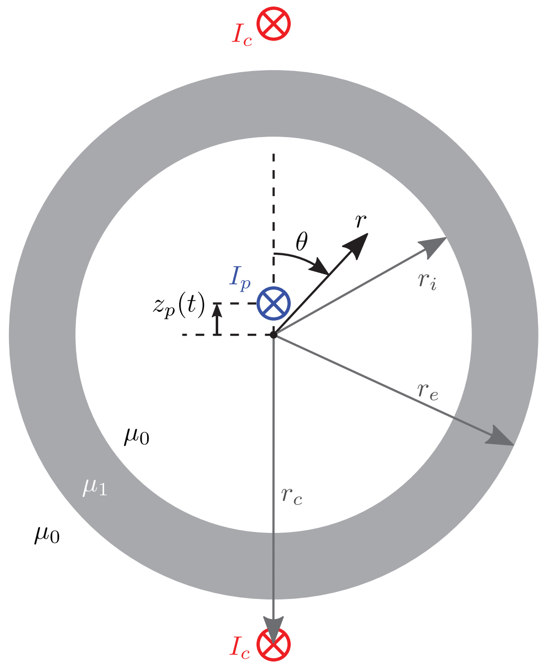

FIG. 1. Schematic of the cylindrical model problem, showing geometry, parameters, and co-ordinates.

As the magnetic flux density is two-dimensional and divergence-free, it may be written using a flux function $\psi(r, \theta, t)$,

$$\boldsymbol{B} = \nabla\psi \times \boldsymbol{e}_\parallel = \frac{1}{r}\frac{\partial \psi}{\partial \theta}\boldsymbol{e}_r - \frac{\partial \psi}{\partial r}\boldsymbol{e}_\theta, \tag{3}$$

where $\boldsymbol{e}_\parallel$, $\boldsymbol{e}_r$, and $\boldsymbol{e}_\theta$ are the unit vectors in the directions of positive I_p, increasing r, and increasing θ, respectively. Then, ψ satisfies a diffusion equation within the conducting wall and Laplace's equation in the vacuum regions,

$$\mu_1 \sigma \frac{\partial \psi}{\partial t} = \nabla^2 \psi \quad (w), \tag{4}$$

$$0 = \nabla^2 \psi \quad (i, e). \tag{5}$$

The boundary conditions (2) across the wall–vacuum interfaces r_i and r_e become

$$\left\langle \frac{\partial \psi}{\partial \theta} \right\rangle = \left\langle \frac{1}{\mu}\frac{\partial \psi}{\partial r} \right\rangle = 0. \tag{6}$$

We identify three separate solution regions: interior to the wall (i), within the thickness of the wall itself (w), and exterior to the wall (e).

© Author(s) 2020

General solutions for the magnetic flux in each region will be matched via the boundary conditions (6).

A. Equilibrium solution

First, we derive the solution when the plasma wire is stationary, which has a flux function $\Psi(r,\theta)$. (From here on, we use the upper-case $(\boldsymbol{B},\Psi)$ for steady solutions and the lower-case $(\boldsymbol{b},\psi)$ for unsteady perturbations.) We refer to this as the "equilibrium" solution—since no motion is involved—but no classical plasma equilibrium (i.e., solution to the Grad–Shafranov equation) is calculated. For the steady case, no current flows in the wall, and the flux function satisfies $\nabla^2\Psi = 0$ everywhere. The solution consists of two distinct portions—the magnetic flux due to the plasma wire $\Psi^{(p)}$ and that due to the divertor coils $\Psi^{(c)}$—which may be linearly superimposed.

1. Plasma wire

We begin with the magnetic flux due to the plasma wire in equilibrium at an arbitrary height z_p, denoted by a superscript (p). Note that, in the vertical stability problem, the plasma is never held stationary at a finite height by definition, and so, the solution with non-zero z_p is inherently unsteady. Nevertheless, the steady field due to a plasma wire at an arbitrary height will prove useful in the following discussion and so is presented below.

First, observe that in the absence of any ferromagnetic effect, it is well known[12] that the solution can be expressed as the series,

$$\Psi^{(p)} = \frac{\mu_0 I_p}{2\pi}\left(-\ln\left(\frac{r_>}{r_i}\right) + \sum_{m=1}^{\infty}\left(\frac{r_<}{r_>}\right)^m \frac{\cos m\theta}{m}\right), \tag{7}$$

where $r_{\lessgtr}$ is the lesser/greater of r and z_p. In the presence of the ferromagnetic wall, since $\Psi^{(p)}$ is still a harmonic function, the general form of the solution is

$$\Psi^{(p)} = \sum_{m=0}^{\infty} \hat{\Psi}^{(p)}_m(r)\cos m\theta, \tag{8}$$

where

$$\hat{\Psi}^{(p)}_0 = -\frac{\mu_0 I_p}{2\pi}\times\begin{cases}\ln(r_>/r_i) & (i)\\ \tilde{\mu}\ln(r/r_i) & (w)\\ \ln(r/r_e) + \tilde{\mu}\ln(r_e/r_i) & (e),\end{cases} \tag{9}$$

$$\hat{\Psi}^{(p)}_{m\geq 1} = C^{(p)}_m\left(\frac{r_i}{r}\right)^m + D^{(p)}_m\left(\frac{r}{r_i}\right)^m, \tag{10}$$

and the coefficients $C^{(p)}_m$, $D^{(p)}_m$ take on different values in the three regions $(i/w/e)$. The boundary conditions (6) have already been applied to the $m=0$ term, but we now approach them for the $m\geq 1$ coefficients. By comparison with (7), the known internal "source" coefficients due to the plasma wire are

$$C^{(p,i)}_m = \frac{\mu_0 I_p}{2\pi m}\left(\frac{z_p}{r_i}\right)^m. \tag{11}$$

Furthermore, as there are no sources outside of the wall (divertor coils being ignored for now), we must have $D^{(p,e)}_m = 0$. The four boundary conditions (6) applied to (10), thus, give a set of simultaneous equations for the remaining coefficients $D^{(p,i)}_m$, $C^{(p,w)}_m$, $D^{(p,w)}_m$, and $C^{(p,e)}_m$, solved in Appendix A 1. Of particular interest here is the horizontal magnetic flux density at the plasma wire location due to the magnetism of the wall to leading order in z_p since this will be proportional to the (destabilizing) vertical Lorentz force exerted on the plasma. We denote this $B^{(p)}_R$, in analogy with the major radial co-ordinate R in a toroidal tokamak geometry, and define it as positive when pointing to the right in Fig. 1. It is

$$B^{(p)}_R \approx \frac{-D^{(p,i)}_1}{r_i} = \frac{-\mu_0 I_p z_p}{2\pi r_i^2}\frac{(r_i/r_e) - (r_e/r_i)}{\frac{\tilde{\mu}-1}{\tilde{\mu}+1}(r_i/r_e) - \frac{\tilde{\mu}+1}{\tilde{\mu}-1}(r_e/r_i)}. \tag{12}$$

If the wall is thin in a geometrical sense, $\delta_w = r_e - r_i \ll r_i$, then this simplifies to

$$B^{(p)}_R \approx \frac{-\mu_0 I_p z_p \delta_w}{4\pi r_i^3}\left(\tilde{\mu} - \frac{1}{\tilde{\mu}}\right). \tag{13}$$

As one might expect, increasing either the wall thickness or the effective magnetic permeability increases the ferromagnetic force which acts on the plasma. It is important to reiterate that these expressions are only valid for a *stationary* plasma wire and therefore represent the destabilizing ferromagnetic force which would act in the limit of a slow-growing instability—in the sense that the growth time is much greater than the resistive wall time—during which the magnetic flux within the wall has time to reconfigure itself and remain close to its quasi-steady value.

2. Divertor coils

The other half of the solution is that due to the divertor coils placed above and below the plasma and exterior to the wall, denoted by the superscript (c). The mathematics is much the same as Sec. II A 1, with a few minor alterations. First, owing to the additional symmetry, only even-m terms contribute, and furthermore, the $m=0$ term is unaltered by the presence of the wall, $\hat{\Psi}^{(c)}_0 = -(\mu_0 I_c/\pi)\ln(r_>/r_i)$. Second, $r_{\lessgtr}$ is now the lesser/greater of r and r_c. Third, the current is now external to the wall, so the known coefficients are

$$D^{(c,e)}_m = \frac{\mu_0 I_c}{\pi m}\left(\frac{r_i}{r_c}\right)^m, \tag{14}$$

and $C^{(c,i)}_m$ must be zero in order to ensure regularity at the origin. We may again solve for a solution of the form (10) using the boundary conditions (6)—see Appendix A 2. The salient result is the vertical gradient of the horizontal magnetic flux density at the origin—although $B^{(c)}_R$ is zero at the origin itself, at a small height z_p above it, we have

$$\begin{aligned} B^{(c)}_R &\approx z_p \left.\frac{\partial B^{(c)}_R}{\partial z}\right|_{z=0} = \frac{-2z_p D^{(c,i)}_2}{r_i^2}\\ &= \frac{-\mu_0 I_c z_p}{\pi r_c^2}\frac{4\tilde{\mu}}{(\tilde{\mu}+1)^2 - (\tilde{\mu}-1)^2(r_i/r_e)^4}. \end{aligned} \tag{15}$$

The quantity $\partial B^{(c)}_R/\partial z|_{z=0}$ times I_p gives the destabilizing force gradient acting on the plasma wire due to the presence of the divertor coils. In the limit of a geometrically thin wall, this becomes

© Author(s) 2020

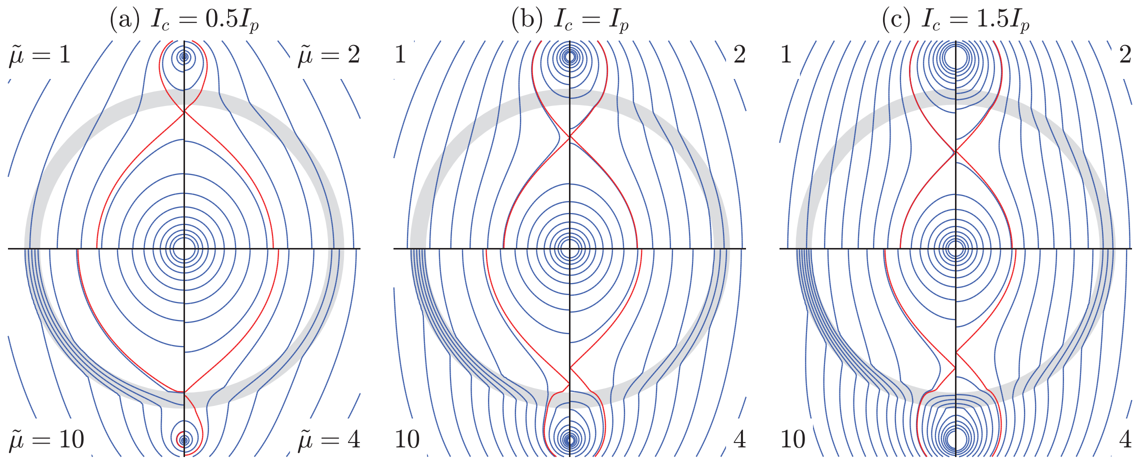

FIG. 2. Example equilibrium configurations in the cylindrical problem with a ferromagnetic wall ($r_i = 0.9r_e$, gray shading) and divertor coils ($r_c = 1.2r_e$). The divertor current I_c varies between the panes [(a) low, (b) intermediate, and (c) high], and the effective relative permeability $\tilde{\mu}$ varies between the quadrants, increasing clockwise from top-left. Flux surfaces (at the same levels in all plots) are shown in blue and the LCFS in red.

$$B_R^{(c)} \approx \frac{-\mu_0 I_c z_p}{\pi r_c^2}\left(1 - \frac{(\tilde{\mu}-1)^2}{\tilde{\mu}}\frac{\delta_w}{r_i}\right), \tag{16}$$

which makes it clear that increasing the magnetic permeability reduces the destabilizing force gradient due to the external coils, by virtue of the magnetic shielding effect.

3. Ferromagnetic effects on the equilibrium

Quite clearly, the presence of the ferromagnetic wall has an effect on the equilibrium magnetic flux distribution. Figure 2 shows some simple equilibria with a plasma wire at the origin and a divertor coil pair carrying various currents I_c. Within each pane, four different equilibria are plotted, for $\tilde{\mu} = [1, 2, 4, 10]$, one in each quadrant. Notice how, as the magnetic permeability is increased, the flux surfaces are increasingly channeled through the wall, reducing their penetration into the interior and allowing expansion of the internal flux surfaces.

To describe the shape of the interior magnetic flux, we introduce the "plasma elongation" κ, defined as the ratio of vertical to horizontal extents of the last closed flux surface (LCFS), which is itself determined either by the location of an internal null (X-point) or the wall inner radius (limited), whichever is closer to the origin. The LCFS is shown as red lines in Fig. 2. Note that, since no attempt is made to treat a distributed plasma current or pressure, this definition of κ is only a proxy for the true plasma elongation, which will depend on the plasma's internal current distribution in addition to the externally applied field.

The equilibrium quantity of most interest to us is the destabilizing force gradient due to the external coils, given in (15). It is well known[13,14] that in the absence of any ferromagnetic effect, this quantity is strongly related to the plasma elongation; we now show that this is still the case in the presence of a ferromagnetic wall. Figure 3 shows plasma elongation as a function of the destabilizing force gradient [$\propto -\mathrm{d}B_R^{(c)}/\mathrm{d}z_p$; see (15)] across a range of parameter values—wall location $r_w = (r_i + r_e)/2$, wall thickness, relative permeability, and divertor current are all varied simultaneously. For the X-point configurations, there is a strong correlation between elongation and the destabilizing force gradient, implying that once the plasma elongation has been specified as a design constraint, so too has the destabilizing force gradient due to the external coils, independent of the existence of any ferromagnetic effect. A larger $\tilde{\mu}$ simply increases the external currents required in order to achieve that elongation, in accordance with (15) or (16). Note, however, that this says nothing about the destabilizing ferromagnetic force (12), which has no such connection to the plasma elongation and increases with $\tilde{\mu}$.

B. Time-dependent solution

We now move our discussion to the time-dependent field due to currents induced in the wall when the plasma is displaced vertically

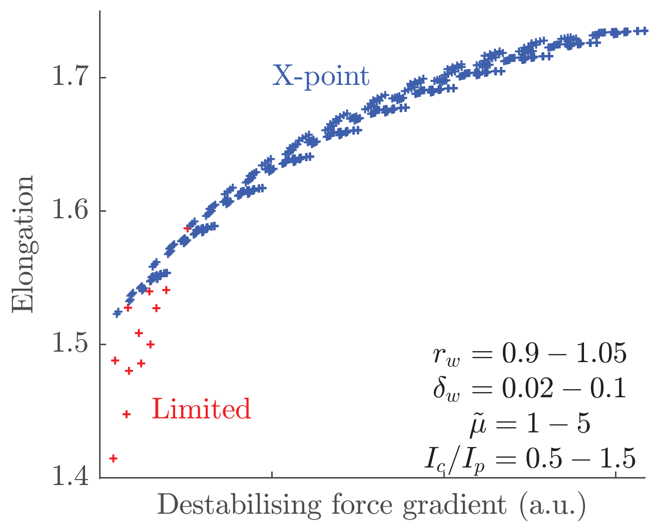

FIG. 3. Elongation of the last closed flux surface as a function of the destabilizing force gradient due to divertor coils (15) for a scan of the wall location, wall thickness, magnetic permeability, and divertor current over the ranges indicated. The divertor coils are at $r_c = 1.2$. Wall-limited cases are shown in red and X-point cases in blue.

© Author(s) 2020

with an instability growth rate γ, that is, $z_p \propto e^{\gamma t}$. In the non-ferromagnetic situation, this force is always stabilizing, and the induced currents in the wall act to slow down the instability. When the wall is ferromagnetic, however, these currents must compete with the destabilizing force due to the magnetic attraction between plasma and the wall, as derived in Sec. II A 1 [Eq. (12)]. Hence, it is not immediately obvious whether the wall will provide a net stabilizing or destabilizing influence when ferromagnetic effects are taken into account.

We proceed to calculate the unsteady flux function $\psi(r,\theta,t)$, which is governed by (4) and (5). In the limit of small plasma displacement, the general solution to leading order in z_p may be written as

$$\psi = \hat{\psi}(r)e^{\gamma t}\cos\theta, \tag{17}$$

where [using Eqs. (6) and (11) of Ref. 11 with $k=0$, $m=1$]

$$\hat{\psi}(r)e^{\gamma t} = \begin{cases} c^{(i)}\left(\dfrac{r_i r_<}{z_p r_>}\right) + d^{(i)}\left(\dfrac{r}{r_i}\right) & (i) \\ c^{(w)}\mathsf{I}_1(y) + d^{(w)}\mathsf{K}_1(y) & (w) \\ c^{(e)}\left(\dfrac{r_i}{r}\right) & (e). \end{cases} \tag{18}$$

Here, $r_{\lessgtr}$ is the lesser/greater of r and z_p, with $\mathsf{I}_1(y)$ and $\mathsf{K}_1(y)$ the modified Bessel functions of order 1 and argument $y = r\sqrt{\mu_1\sigma\gamma}$. Lower case is used for the coefficients $c^{(\cdot)}$ and $d^{(\cdot)}$ to emphasize that they are part of the time-dependent solution; by comparison with (11), we can see that $c^{(i)} = \mu_0 I_p z_p/2\pi r_i$ is known, but the remaining coefficients must be determined from the boundary conditions (6). (Note that $d^{(e)}=0$ to ensure regularity as $r\to\infty$.) This is done in Appendix A 3; the resulting horizontal magnetic flux at the origin, tantamount to the unsteady Lorentz force exerted on the plasma, is

$$b_R = -\frac{\mu_0 I_p z_p}{2\pi r_i^2}\frac{d^{(i)}}{c^{(i)}}, \tag{19}$$

with $d^{(i)}/c^{(i)}$ from (A18). For a given geometry, the reactive force acting back on the plasma due to the wall depends in a non-trivial way upon the instability growth rate γ and the wall's effective magnetic permeability μ_1; this is shown by the solid lines in Fig. 4. As the growth rate (which is normalized to the non-ferromagnetic wall time $\tau_{w0} = \mu_0\sigma\delta_w^2$) increases, so too does the stabilizing wall force as a result of the larger currents induced within the wall. If the wall is ferromagnetic, this force is decreased with respect to the $\tilde{\mu}=1$ case, such that it even becomes negative (i.e., destabilizing rather than stabilizing) at smaller values of γ—this emulates previous studies into the dependence of FRWMs on rotation frequency.[15,16] The asymptote as $\gamma\tau_{w0}\to 0$ is shown by the horizontal dotted lines, calculated using the solution (12) for a plasma wire held stationary at a height z_p. Hence, if the instability growth rate is slow compared to the wall time, such that the internal magnetic flux evolves in a quasi-steady manner, then the effect of ferromagnetism is to provide an additional destabilizing force, one which is not associated with the equilibrium magnetic flux configuration and therefore does not come with the dividend of an increase in plasma elongation.

If the instability growth rate is large compared to the wall time, however, the story is somewhat different. In this case, the magnetic

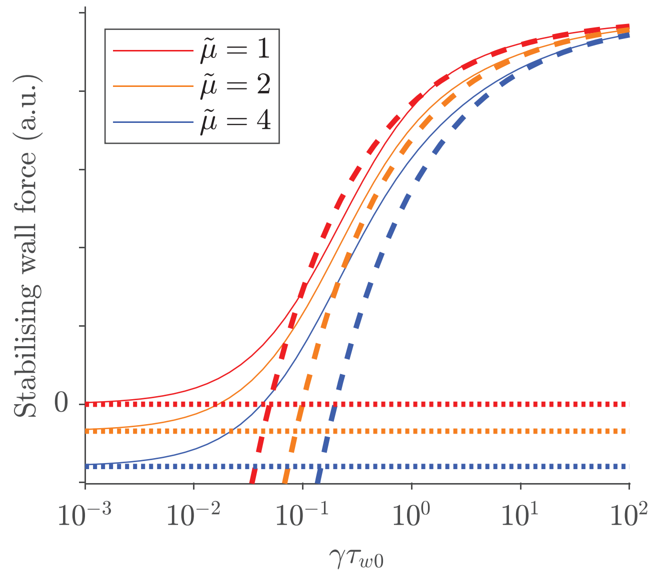

FIG. 4. Force due to the wall as a function of the instability growth rate for different $\tilde{\mu}$. The geometry is as Fig. 3 ($r_i = 0.9r_e$). Dashed lines show the "thick-wall" (large γ) limit given by (20) and dotted lines the thin-wall (small γ) limit given by (12).

skin depth $s\sim(\mu_1\sigma\gamma)^{-1/2}$ is much less than the wall thickness, and so, the choice of r_e is in practice irrelevant. Regularity at infinity then demands $c^{(w)}=0$ and so the expression for b_R simplifies to

$$\begin{aligned} b_R &\approx \frac{\mu_0 I_p z_p}{2\pi r_i^2}\frac{y_i\mathsf{K}_0(y_i) - (\tilde{\mu}-1)\mathsf{K}_1(y_i)}{y_i\mathsf{K}_0(y_i) + (\tilde{\mu}+1)\mathsf{K}_1(y_i)} \\ &\approx \frac{\mu_0 I_p z_p}{2\pi r_i^2}\left(1 - \frac{2\tilde{\mu}}{y_i} + \mathcal{O}(y_i^{-2})\right), \end{aligned} \tag{20}$$

where the latter form is the limit as $y_i\to\infty$ ($s \ll r_i$). This is plotted as dashed lines in Fig. 4. It is important to notice that the above expression depends on γ and $\tilde{\mu}$ only through the term

$$\frac{y_i}{\tilde{\mu}} = r_i\sqrt{\frac{\mu_0\sigma\gamma}{\tilde{\mu}}}, \tag{21}$$

and so they only enter the stabilizing force in the combination $\gamma/\tilde{\mu}$. This suggests that, for a given destabilizing force gradient, growth rates will be larger by a factor $\tilde{\mu}$ for ferromagnetic cases in which the wall may be considered magnetically thick; this result is the same as Ref. 11 for FRWMs.

Note that, regardless of the value of $\tilde{\mu}$, there is maximum possible b_R equal to the ideal-wall value $b_{R,\max} = \mu_0 I_p z_p/2\pi r_i^2$, which is reached in the limit of the infinite growth rate. This means that if the magnitude of the destabilizing force due to external coils [$B_R^{(c)}$, Eq. (15)] is greater than $b_{R,\max}$, then the conducting wall alone is insufficient to slow the instability to sub-Alfvénic speeds, meaning that the equilibrium is ideally unstable.

C. Calculation of the growth rate

Having now derived both the equilibrium and time-dependent Lorentz forces acting on the plasma wire, we proceed to calculate the

© Author(s) 2020

instability growth rate γ as a function of the problem parameters. We consider a plasma of negligible mass whose vertical position increases exponentially but nevertheless always remains close to the origin such that the problem may be linearized. Since the plasma is massless, the total vertical Lorentz force at its location must be zero, or equivalently

$$B_R^{(c)} + b_R = 0, \tag{22}$$

where $B_R^{(c)}$ comes from (15) and b_R from (19). This condition of force-free plasma motion may be solved numerically for the growth rate γ; example curves of the growth rate vs the destabilizing force gradient are given in Fig. 5. As suggested by the discussion of Sec. II B, there is a dichotomy between fast- and slow-growing instabilities, and so we treat the two extremes separately below.

1. Fast (thick wall) instability

The fast limit of (22) is characterized by a magnetic skin depth which is much less than the thickness of the wall ($s \ll \delta_w$), or equivalently a growth rate much greater than the resistive wall time ($\gamma\tau_{w0} \gg 1$). Because the skin effect predominates, the internal magnetic flux is relatively slow to react to the motion of the plasma wire, and the destabilizing ferromagnetic effect of the *equilibrium* solution in Sec. II A 1 is not felt by the plasma. Hence, the destabilizing influence is purely due to the existence of the divertor coils, and the impact of ferromagnetism is solely a reduction in the magnitude of the stabilizing wall force (19). In particular, b_R is given by the limiting form (20), which, as discussed there, is a function of γ and $\tilde{\mu}$ only in the combination $\gamma/\tilde{\mu}$. The external destabilizing force $B_R^{(c)}$ [Eq. (15)], despite ostensibly depending on the magnetic permeability, is fixed by the plasma elongation as discussed in Sec. II A 3. Hence, for a given elongation, growth rates are inflated by a factor $\tilde{\mu}$ relative to the non-ferromagnetic case in situations where the wall is thicker than the magnetic skin depth; this is evidenced in Fig. 5(a), which shows a coalescence of the curves of $\gamma/\tilde{\mu}$ vs $B_R^{(c)}$ for $\gamma\tau_{w0} \gtrsim 1$, as they asymptote toward the ideal stability limit.

2. Slow (thin wall) instability

At the opposite extreme, we have the slow limit, for which the instability growth rate is much less than the wall time ($\gamma\tau_{w0} \ll 1$), which amounts to a magnetic skin depth much greater than the wall thickness. Hence, the perturbation due to the motion of the plasma occupies the whole volume of the conducting wall, and the interior field has time to adjust on account of the ferromagnetic effects of the wall. The destabilizing force acting on the plasma is then a sum of that due to the divertor coils (15) and ferromagnetic wall (12). The stabilizing effect of the currents induced in the wall, on the other hand, is independent of its magnetic permeability in this limit, as shown in Appendix B. Hence, the curves of γ against the *total* destabilizing force gradient plotted in Fig. 5(b) converge for $\gamma\tau_{w0} \lesssim 1$. The interpretation here is that the instability growth rate also increases due to the ferromagnetic effect in the case of a thin wall, although the dependence of γ on $\tilde{\mu}$ is less trivial since it enters through the destabilizing term (12). In fact, in the limiting case $\delta_w \ll s \ll r_w$, the force balance (22) becomes [see Appendix B and Eq. (13)]

$$\frac{\mu_0 I_p z_p}{2\pi r_w^2}\left(1 + \frac{2}{\mu_0\sigma\gamma\delta_w r_w}\right)^{-1} + B_R^{(c)} - \frac{\mu_0 I_p z_p \delta_w}{4\pi r_w^3}\left(\tilde{\mu} - \frac{1}{\tilde{\mu}}\right) \approx 0. \tag{23}$$

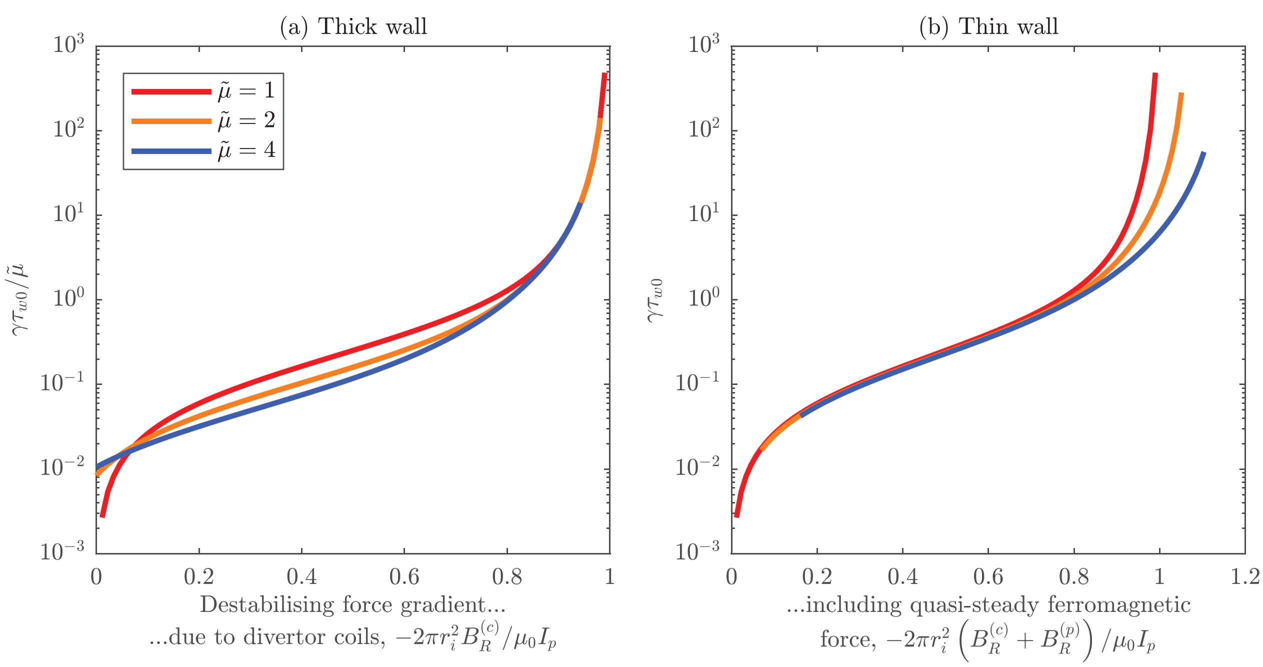

FIG. 5. Vertical instability growth rate as a function of the destabilizing force acting on the plasma, either (a) due to the external coils alone [Eq. (15)] or (b) including the quasi-steady ferromagnetic force as well [Eq. (12)]. The former collapse in the limit of a thick wall, $\gamma\tau_{w0} \gg 1$ (note that the vertical axis is scaled by $\tilde{\mu}$), whereas the latter collapse for a thin wall, $\gamma\tau_{w0} \ll 1$. Geometry is as Fig. 2, and the coil current I_c varies between 0 and I_p.

© Author(s) 2020

Solving for the growth rate, we get

$$\gamma\tau_{w0} \approx \frac{\delta_w}{r_w}\left[\left(\frac{\delta_w}{r_w}\left(\tilde{\mu}-\frac{1}{\tilde{\mu}}\right)-\frac{4\pi r_w^2 B_R^{(c)}}{\mu_0 I_p z_p}\right)^{-1}-\frac{1}{2}\right]^{-1}. \quad (24)$$

As discussed previously, in order to maintain a specified plasma elongation in the presence of ferromagnetic material, the divertor coil current I_c must be increased such that $B_R^{(c)}$ is unchanged [in accordance with (15) or its approximation (16)], and hence, the term containing $B_R^{(c)}$ in (24) can be thought of as independent of $\tilde{\mu}$. This expression, therefore, captures the dependence of the growth rate on the effective magnetic permeability (and wall geometry) at fixed plasma elongation, for the important limit of a (magnetically *and* geometrically) thin wall.

Making further use of the fact that $\delta_w \ll r_w$, we may usefully recast (24) in terms of γ_0, the growth rate in the absence of any ferromagnetic effect,

$$\gamma\tau_{w0} \approx \gamma_0\tau_{w0} + \left(\tilde{\mu}-\frac{1}{\tilde{\mu}}\right)\left(\frac{\delta_w}{r_w}+\frac{\gamma_0\tau_{w0}}{2}\right)^2. \quad (25)$$

This relation is plotted as the dashed curves in Fig. 6(a), along with both the exact solution (as a solid line) and the opposite limit $\gamma\tau_{w0} \gg 1$ of Sec. II C 1. It appears that the exact solution is well-approximated by (25) for $\gamma_0\tau_{w0} \lesssim 1$ and $\gamma = \tilde{\mu}\gamma_0$ for $\gamma_0\tau_{w0} \gtrsim 1$, particularly at the smaller values of $\tilde{\mu}$ applicable to tokamaks. This scheme, therefore, provides a simple means by which to adjust the values of growth rates calculated for a conventional conducting wall in order to account for the effects of ferromagnetism.

As we can see from Fig. 6(b), the effect is, in general, to increase growth rates by a factor on the order of the effective relative magnetic permeability $\tilde{\mu}$. The factor can be much larger than $\tilde{\mu}$ for instabilities with $\gamma_0\tau_{w0} \ll 1$, but this is a result of $\gamma_0 \to 0$ rather than $\gamma \to \infty$ and therefore not particularly worrying; physically, this represents the limit of the divertor coils being turned off, so the only destabilizing influence is ferromagnetic, in which case the growth rates are very slow anyway. The effect of ferromagnetism will be most pertinent for the fast, skin-effect dominated solutions, for which the vertical instability growth rate is already large ($\gamma_0\tau_{w0} \gtrsim 1$, i.e., $s \lesssim \delta_w$) but becomes even larger by a factor $\tilde{\mu}$, which could be ~ 2 in future tokamaks.

The conclusions of Ref. 11 are that γ is independent of $\tilde{\mu}$ for $\gamma\tau_{w0} \ll 1$. Mathematically, this is because Ref. 11 neglected the ferromagnetic modification to the drive (their Δg_μ) on the grounds it is much smaller than the drive itself (their g_m). Since that study focused on thin-walled tokamaks ($r_w \sim 50\delta_w$ in line with present devices), this is practicable, but may not hold for the large quantities of ferritic material envisaged in reactor-type machines, particularly in weakly driven ($g_m \ll 1$) situations. Physically, the reason our slow solutions are further destabilized for $\tilde{\mu} > 1$ is the presence of the quasi-steady ferromagnetic force, which is a part of (19) but isolated in (12).

III. SPHERICAL TOKAMAK MODEL PROBLEM

Our second model problem considers an axisymmetric tokamak with the ferromagnetic conducting wall now taken to be a spherical shell which completely encloses the plasma. This choice is motivated by the need for a greater understanding of ferromagnetic effects in spherical tokamaks, particularly their vertical stability characteristics at exaggerated elongations, acknowledging the importance of balancing divertor loads in double-null configurations[8,17] and avoiding disruptions. If ferromagnetic materials are to be used for tritium breeding modules, then these will have to be placed on the low-field side only in a spherical tokamak,[18] a feature which this model emulates. Even in a

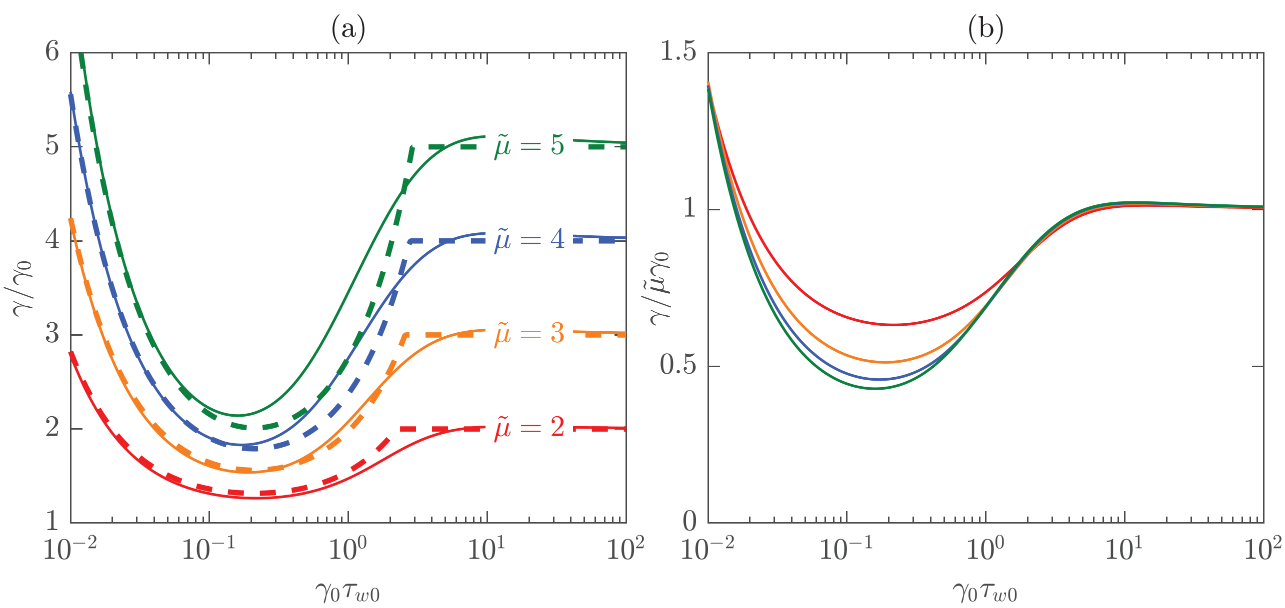

FIG. 6. (a) Relative change in vertical instability growth rate γ as a function of its value in the absence of any ferromagnetic effects, γ_0, keeping the externally applied destabilizing force gradient (and thus plasma elongation) constant. Solid lines show the exact result and dashed lines the limiting forms for $\gamma\tau_{w0} \ll 1$ [see (25)] and $\gamma\tau_{w0} \gg 1$ ($\gamma = \tilde{\mu}\gamma_0$). (b) Exact result again but scaled by $\tilde{\mu}$. The geometry is as Fig. 2.

© Author(s) 2020

conventional tokamak, simple geometrical considerations imply that more ferromagnetic steel is likely to be located on the outboard side—say, for the structural components of tritium breeding modules[3] or toroidal field ripple reducing inserts[5,6]—so this model problem provides useful insight in this context too.

It is to be expected that the paradigm of Sec. II, which makes a distinction between thick- and thin-walled instabilities, will carry over to this section as well, and indeed we will show this to be broadly the case. There are, however, a few new results that emerge in this second model problem, particularly with respect to the plasma's radial equilibrium, and subtleties associated with the evaluation of the destabilizing force on the plasma wire. This model is also much more flexible, with a range of plasma and coil locations possible, and should—by virtue of being axisymmetric rather than planar—have greater predictive capability. Since this model is very closely related to that of Sec. II, we proceed by analogy with the thread of that section, highlighting significant differences and new results when they arise. Symbols will be extensively re-used and have very similar meanings to Sec. II, being differentiated only by context. We also append certain equations with (cf. $\sim$) labels, which relate them to analogous expressions in Sec. II.

The problem schematic is shown in Fig. 7. Since the wall is a spherical shell, the obvious co-ordinate system is spherical polars (r, θ, ϕ) with r the radial distance and θ the poloidal angle; the toroidal angle ϕ is ignorable because axisymmetry is assumed. We will use these interchangeably with cylindrical polar co-ordinates (R, z, ϕ) aligned with the symmetry axis. The ferromagnetic wall is again given a constant effective magnetic permeability, although this is now a fairly crude approximation because of the significant $1/R$ variation of the toroidal field in (1). (The choice is justified if the wall currents are concentrated on the outboard side, however.) The circular plasma wire has radius R_p, and its vertical position z_p is assumed small; this plasma model is also used in Ref. 19. Poloidal field coils are introduced outside of the conducting wall in up-down symmetric pairs, one example of which is shown in Fig. 7, but many such pairs may be included as desired. By convention, all currents are positive in the direction of increasing ϕ (into the page).

Rather than the flux function ψ of Sec. II, we now work with the vector potential $A(r, \theta, t)\boldsymbol{e}_\phi$ such that the poloidal flux density is

$$\boldsymbol{B} = \nabla \times (A\boldsymbol{e}_\phi) = \frac{1}{r\sin\theta}\frac{\partial}{\partial\theta}(A\sin\theta)\boldsymbol{e}_r - \frac{1}{r}\frac{\partial}{\partial r}(rA)\boldsymbol{e}_\theta \tag{26}$$

(cf. 3) in which case the boundary conditions (2) at $r_{i,e}$ become

$$\left\langle \frac{\partial}{\partial\theta}(A\sin\theta)\right\rangle = \left\langle \frac{1}{\mu}\frac{\partial}{\partial r}(rA)\right\rangle = 0 \tag{27}$$

(cf. 6). Note also that the partial differential equation governing A is

$$\mu\sigma\frac{\partial A}{\partial t} = \frac{1}{r^2}\frac{\partial}{\partial r}\left(r^2\frac{\partial A}{\partial r}\right) + \frac{1}{r^2}\frac{\partial}{\partial\theta}\left(\frac{1}{\sin\theta}\frac{\partial}{\partial\theta}(A\sin\theta)\right) \tag{28}$$

(cf. 4). As before, our approach is to first calculate the equilibrium field, which informs the destabilizing force, and then the stabilizing time-dependent field due to the displacement of the plasma wire vertically as $e^{\gamma t}$. Assuming a massless plasma, the net Lorentz force from these two fields must vanish at its location, a criterion that gives an equation for the instability growth rate γ.

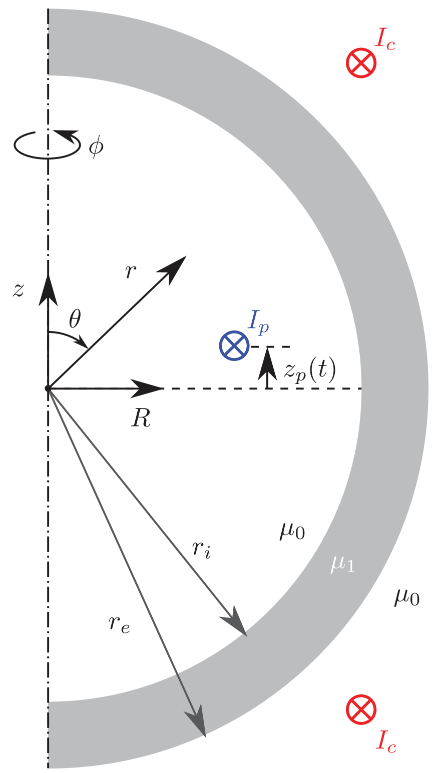

FIG. 7. Schematic of the spherical model problem, showing geometry, parameters, and co-ordinates.

A. Equilibrium solution

We begin by solving for the equilibrium magnetic flux density, which satisfies the steady version of (28) subject to the boundary conditions (27). Again, contributions due to the plasma wire and external coil pairs may be treated independently and then summed.

1. Plasma wire

We first derive the solution due to the plasma wire at an arbitrary cylindrical radius R_p and height z_p (equivalently, spherical radius r_p and poloidal angle θ_p), in analogy with Sec. II A 1. In the absence of any ferromagnetic effects, the vector potential due to a thin circular hoop carrying a constant current, which zeros the right-hand side of (28), may be written as the infinite sum,[10]

$$A^{(p)} = \sum_{\ell=1}^{\infty}\frac{\mu_0 I_p\sin^2\theta_p}{2\ell(\ell+1)}\frac{r_p r_<^\ell}{r_>^{\ell+1}}P_\ell^1(\cos\theta)P_\ell^1(\cos\theta_p) \tag{29}$$

(cf. 7), where $r_\lessgtr$ is the lesser/greater of r and r_p, and $P_\ell^1(\cdot)$ is the associated Legendre polynomial of degree ℓ and order 1. Introducing the ferromagnetic wall, we then have the general solution

$$A^{(p)} = \sum_{\ell=1}^{\infty}\hat{A}_\ell^{(p)}(r)P_\ell^1(\cos\theta) \tag{30}$$

(cf. 8), where

© Author(s) 2020

$$\hat{A}_\ell^{(p)} = C_\ell^{(p)} \frac{r_i^{\ell+1} r_<^\ell}{r_p^\ell r_>^{\ell+1}} + D_\ell^{(p)} \left(\frac{r}{r_i}\right)^\ell \tag{31}$$

(cf. 10). The coefficients $C_\ell^{(p)}$ and $D_\ell^{(p)}$ take on different values in the three domains $(i/w/e)$; we can see by comparison with (29) that the known internal coefficients are

$$C_\ell^{(p,i)} = \frac{\mu_0 I_p \sin^2\theta_p}{2\ell(\ell+1)} \left(\frac{r_p}{r_i}\right)^{\ell+1} P_\ell^1(\cos\theta_p) \tag{32}$$

(cf. 11), and furthermore any valid solution must vanish at infinity, implying $D_\ell^{(p,e)} = 0$. The remaining coefficients are solved for in Appendix C 1 by application of the boundary conditions (27). A simple example magnetic flux distribution is shown in Fig. 8, with a comparison to the non-ferromagnetic solution.

Having derived the vector potential due to the reaction of the ferromagnetic wall to the plasma wire, the next step is to evaluate the magnetic flux components at the location of the plasma itself since they will give the resulting Lorentz force acting upon it. The natural choice of equilibrium is a symmetric one in which the plasma wire is sited in the midplane, $z_p = 0$, in which case the vertical field at the plasma location is

$$B_z^{(p)}\Big|_{\substack{R=R_p \\ z=z_p=0}} = \sum_{\substack{\ell=1 \\ \ell\ \mathrm{odd}}}^{\infty} \frac{\mu_0 I_p}{2\ell R_p} \frac{D_\ell^{(p,i)}}{C_\ell^{(p,i)}} \left(\frac{R_p}{r_i}\right)^{2\ell+1} \left[P_\ell^1(0)\right]^2, \tag{33}$$

with $D_\ell^{(p,i)}/C_\ell^{(p,i)}$ from (C6). Clearly, unlike the cylindrical model, the equilibrium field due to the ferromagnetic wall has a non-zero vertical component at the plasma location and hence exerts a horizontal force upon it, with a sign such that the two attract each other (i.e., the wall pulls the plasma radially outward). We postpone discussion of the effect of this on plasma equilibrium to Sec. III A 3 once the external coil fields have been evaluated.

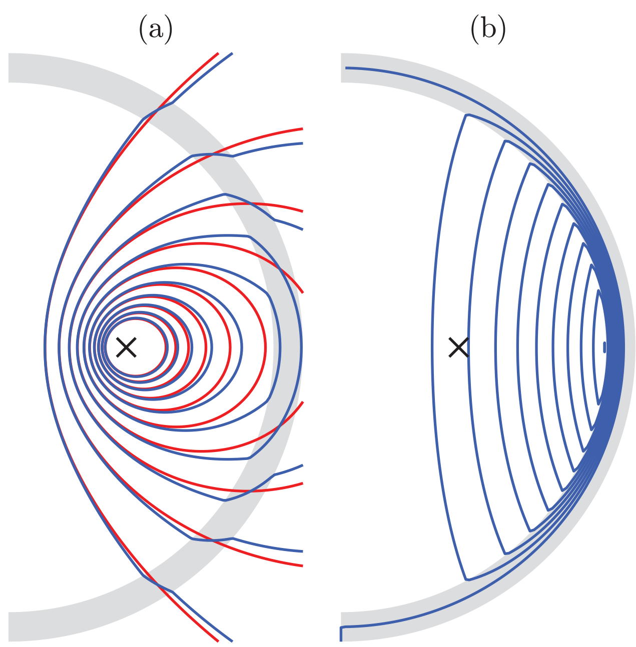

FIG. 8. Equilibrium magnetic flux surfaces due to a plasma wire. (a) Comparison between ferromagnetic ($\tilde{\mu} = 3$, blue) and non-ferromagnetic ($\tilde{\mu} = 1$, red) cases. (b) Difference between the two, i.e., the field "due to the wall." Geometry is $r_i = 0.9r_e$, $R_p = 0.4r_e$, and $z_p = 0$; the black cross represents the plasma wire.

Because our equilibrium is symmetric about the midplane, the radial magnetic flux at the plasma location is zero and hence there is no vertical Lorentz force acting on the plasma in equilibrium. However, when the plasma wire is displaced vertically by a small amount (i.e., at the onset of a VDE), it will experience a vertical force as a result of the equilibrium field described above and in Appendix C 1 (ignoring induced currents in the wall for the time being). To leading order in the plasma height z_p, this can be separated into two components. The first is due to the curvature of the equilibrium field produced by the ferromagnetic wall—see the field lines of Fig. 8(b). It is

$$\frac{\partial}{\partial z}\left(B_R^{(p)}\Big|_{\substack{R=R_p \\ z_p=0}}\right)_{z=0} = \sum_{\substack{\ell=3 \\ \ell\ \mathrm{odd}}}^{\infty} \frac{\mu_0 I_p(\ell-1)}{2\ell R_p^2} \frac{D_\ell^{(p,i)}}{C_\ell^{(p,i)}} \times \left(\frac{R_p}{r_i}\right)^{2\ell+1} \left[P_\ell^1(0)\right]^2. \tag{34}$$

This contribution is not present in the cylindrical model of Sec. II A 1 because the equilibrium field due to the wall is zero at the origin when $z_p = 0$. Its effect here is always vertically stabilizing—as is evident from Fig. 8(b), considering that the direction of magnetic flux must be such that the horizontal force on the plasma is radially outward—but because the force arises from field line curvature, this stabilization comes at the cost of reduced plasma elongation. Note that this contribution is also independent of the instability growth rate and so is most simply thought of as a modification to the external coils' destabilizing force gradient.

The second contribution, which is familiar from the cylindrical problem (Sec. II A 1), is only present in the limit of a slow-growing (or thin-wall, $\gamma\tau_{w0} \ll 1$) instability. It is the change in the equilibrium radial field in the midplane ($z = 0$) due to a slight excursion of the plasma wire from $z_p = 0$, which is

$$\frac{\partial}{\partial z_p}\left(B_R^{(p)}\Big|_{\substack{R=R_p \\ z_p=0}}\right)_{z_p=0} = \sum_{\substack{\ell=2 \\ \ell\ \mathrm{even}}}^{\infty} -\frac{\mu_0 I_p \ell(\ell+1)}{2R_p^2} \frac{D_\ell^{(p,i)}}{C_\ell^{(p,i)}} \times \left(\frac{R_p}{r_i}\right)^{2\ell+1} \left[P_\ell^0(0)\right]^2 \tag{35}$$

(cf. 12)—observe the subtle difference between the derivatives in (34) and (35). This represents the additional destabilizing force due to the effects of ferromagnetism in the case $\gamma\tau_{w0} \ll 1$, as discussed in Sec. II C 2, which [unlike the first component (34)] is not directly linked to the plasma elongation. If the wall is also geometrically thin ($\delta_w \ll r_i$) and we may approximate the sum in (35) by the first two terms only on the grounds that the plasma wire is reasonably far from the wall, then we may use (C7) to find

$$\Delta\hat{n} = -\frac{R_p}{B_z}\frac{\partial}{\partial z_p}\left(B_R^{(p)}\Big|_{\substack{R=R_p \\ z_p=0}}\right)_{z_p=0} \approx \frac{3}{10}\frac{\mu_0 I_p}{B_z R_p}\left(\frac{R_p}{r_i}\right)^5 \frac{\delta_w}{r_i}\Delta_\mu \tag{36}$$

(cf. 13), where

© Author(s) 2020

$$\Delta_\mu = \left(1 - \frac{1}{\tilde{\mu}}\right)\left[(2\tilde{\mu}+3) + \frac{25}{12}(4\tilde{\mu}+5)\left(\frac{R_p}{r_i}\right)^4\right]. \tag{37}$$

Note that (36) has a very strong dependency upon the distance between the plasma and wall (i.e., R_p/r_i) and that we have expressed it as a modification $\Delta\hat{n}$ to the field index $\hat{n}$. Tsuzuki *et al.*[20] reported a relative change in this value of a few percent due to the ferromagnetic wall when the plasma is slightly displaced vertically. Using relevant parameters for the JFT-2M tokamak [$r_i \approx 1.7$ m, $R_p \approx 1.3$ m, $\delta_w \approx 8$ mm, $\tilde{\mu} \sim 2-4$, and (from Ref. 21) $\xi \sim 0.2-0.7$], we consistently estimate $\Delta\hat{n}/\hat{n} \sim 0.4-3.6\%$ using the above expression.

2. External coils

The equilibrium field due to an external coil pair is comparatively straightforward. The general solution is very similar to (31), only now with a source external to the wall,

$$\hat{A}_\ell^{(c)} = C_\ell^{(c)}\left(\frac{r_i}{r}\right)^{\ell+1} + D_\ell^{(c)}\frac{r_c^{\ell+1}r_<^\ell}{r_i^\ell r_>^{\ell+1}}, \tag{38}$$

where $r_\lessgtr$ is the lesser/greater of r and r_c and the coefficients take on different values in the various domains. For regularity at the origin, all $C_\ell^{(c,i)}$ coefficients must be zero, whereas the external coefficients are

$$D_\ell^{(c,e)} = \frac{\mu_0 I_c \sin^2\theta_c}{\ell(\ell+1)}\left(\frac{r_i}{r_c}\right)^\ell P_\ell^1(\cos\theta_c) \tag{39}$$

(cf. 14) for ℓ odd, and zero for ℓ even. The solution for the remaining coefficients is given in Appendix C 2. The vertical component of magnetic flux density at the plasma location is

$$B_z^{(c)}\Big|_{\substack{R=R_p\\z=0}} = \sum_{\substack{\ell=1\\\ell\text{ odd}}}^{\infty}\frac{\mu_0 I_c \sin^2\theta_c}{\ell R_p}\frac{D_\ell^{(c,i)}}{D_\ell^{(c,e)}}\left(\frac{R_p}{r_c}\right)^\ell P_\ell^1(\cos\theta_c)P_\ell^1(0), \tag{40}$$

with $D_\ell^{(c,i)}/D_\ell^{(c,e)}$ from (C13). Through this term, external coils may exert a force upon the plasma in order to maintain the radial equilibrium. As for vertical stability, the force gradient is provided by the curvature term

$$\frac{\partial B_R^{(c)}}{\partial z}\Big|_{\substack{R=R_p\\z=0}} = \sum_{\substack{\ell=3\\\ell\text{ odd}}}^{\infty}\frac{\mu_0 I_c(\ell-1)\sin^2\theta_c}{\ell R_p^2}\frac{D_\ell^{(c,i)}}{D_\ell^{(c,e)}} \times\left(\frac{R_p}{r_c}\right)^\ell P_\ell^1(\cos\theta_c)P_\ell^1(0) \tag{41}$$

(cf. 15). Note that this term may be stabilizing, destabilizing, or neutral depending on the precise location of the external coil pair and sign of I_c.

3. Radial force balance

Whereas the cylindrical model problem of Sec. II was trivially in force equilibrium before the VDE, by virtue of the externally applied magnetic flux being zero at the origin, for the spherical version the equilibrium configuration must obey a radial force balance. That is, the plasma hoop force and ferromagnetic pull of the wall (both of which act radially outward) must be balanced by the externally applied vertical field,

$$B_z^{hoop} + B_z^{(p)} + \sum_c B_z^{(c)} = 0, \tag{42}$$

wherein the plasma and coil fields come from (33) and (40), respectively, and we have allowed for the inclusion of multiple external coils. In the limit of a large aspect ratio plasma (taken for a simple order-of-magnitude estimate), the vertical field required to balance the plasma hoop force is[22]

$$B_z^{hoop} = \frac{\mu_0 I_p}{4\pi R_p}\left(\ln\frac{8R_p}{a_p} + \Lambda - \frac{1}{2}\right), \tag{43}$$

where a_p is the plasma minor radius and $\Lambda = \beta_{pol} + \frac{1}{2}l_i - 1$ for a plasma of poloidal beta β_{pol} and internal inductance l_i; for simplicity, the bracketed quantity in (43) is assumed independent of R_p, and we take nominal values of the various plasma parameters within it—see the caption of Fig. 9—in order to generate a plausible hoop force. (Note that strictly these parameters are not defined for a plasma wire, but the results will prove useful despite this contradiction.)

We explore modification of the radial force balance by means of a simple example, in which both the current in a single external coil pair and the plasma radius R_p are varied in search of equilibrium solutions. We choose a wall with $r_i = 0.9r_e$ and $\tilde{\mu} = 3$, with the external coils placed as a Helmholtz pair at $R_c = 1.2r_e$, $z_c = \pm 0.6r_e$. Figure 9 shows the left-hand side of the force balance (42) as a function of R_p for various coil currents I_c; this quantity is zero in equilibrium. Dashed

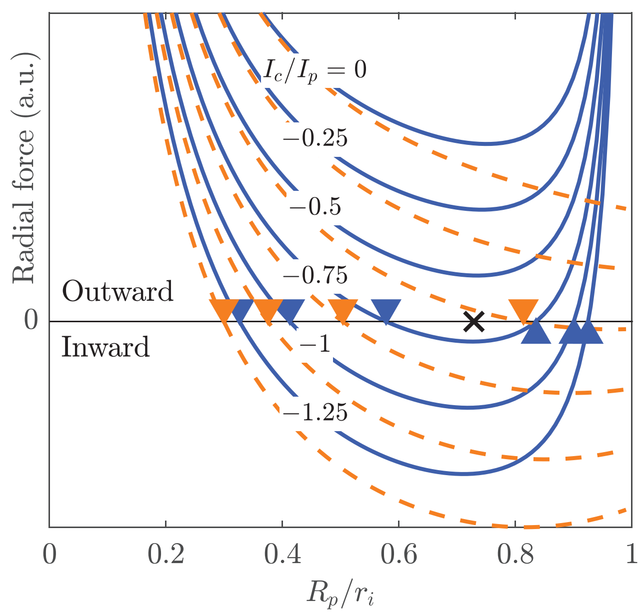

FIG. 9. The net radial force on the plasma (42) as a function of the major radius at various values of external coil current I_c. The parameters are $r_i = 0.9r_e$, $R_c = 1.2r_e$, $z_c = \pm 0.6r_e$, $\tilde{\mu} = 3$, and we use $\Lambda = 0.25$, $R_p/a_p = 2$. Solid blue lines show the ferromagnetic case, with dashed orange lines the $\tilde{\mu} = 1$ equivalent for comparison. Triangles denote equilibria: downward-pointing for stable and upward for unstable. The black cross is the maximum stable equilibrium. Labels "outward" and "inward" indicate the direction of the net force.

© Author(s) 2020

orange lines show the non-ferromagnetic ($\tilde{\mu} = 1$) case for comparison. First consider the topmost pair of lines, with no externally applied field. The non-ferromagnetic case is just (43), which drops off as $1/R_p$, whereas the ferromagnetic case deviates as R_p approaches r_i due to the addition of the $B_z^{(p)}$ term (33), with the outward force on the plasma increasing considerably as it is pulled toward the wall. Since both forces are outward, an equilibrium is unachievable. Addition of an external field with I_c negative, however, pushes the plasma inward, i.e., lowers the curves in Fig. 9 to such a point that solutions to (42) may exist. These are indicated by filled triangles. In the non-ferromagnetic case, there is only ever one such equilibrium, which moves inward as $|I_c|$ increases. If the wall is ferromagnetic, for a given I_c this first equilibrium either moves slightly outward (see the curves for $|I_c| \geq 0.75 I_p$) or ceases to exist at all (see the curves for $I_c = -0.5 I_p$). Furthermore, a second equilibrium comes into being at larger R_p (denoted by upward-pointing triangles), but it is unstable because a small displacement either outward or inward from the equilibrium R_p would result in a net force on the plasma which reinforces that motion. Clearly, in the ferromagnetic case, there is a maximum possible R_p—or equivalently, a minimum requirement on $|I_c|$—for stable equilibrium solutions to exist. (In this example, these are $0.729 r_i$ and $0.674 I_p$, respectively—see the black cross in Fig. 9.) Note that equilibria with R_p just below this value are likely to be metastable; although linearly stable to small displacements, a larger outward perturbation could take the plasma past the unstable equilibrium location, thereby causing it to be pulled inexorably into the wall by their mutual ferromagnetic attraction.

A natural next question is, how might equilibria with a distributed plasma current be affected by significant amounts of ferromagnetic material on the outboard side? Although a full answer to this question is beyond our scope (but see existing discussions of the modification of plasma shape by a ferromagnetic core[23,24] and its inclusion in equilibrium reconstruction[25–27]), it appears that currents flowing close to the wall would be strongly attracted toward it. This may place a limit on how close the LCFS could get to the ferromagnetic wall, particularly for plasmas of low internal inductance.

4. Ferromagnetic equilibria

We are now in a position to calculate the equilibrium magnetic flux from both a plasma wire and a number of external coil pairs. Figure 10 shows a few examples for a reasonably thick wall of moderate effective magnetic permeability. A minimal external coil set is used, with "vertical field" coils on the outboard side providing the bulk of the radial force and "divertor" coils directly above and below the plasma wire controlling the elongation. The current I_c^{div} in the latter pair is varied between the panes of Fig. 10 in order to produce different field shapes; note how the LCFS encloses a smaller area as I_c^{div} increases but also that its elongation κ increases. [A nominal inboard limiter has been included to keep the plasma shape plausible—see Fig. 10(a).] As found in the cylindrical equilibrium (Sec. II A 3), elongation is strongly correlated with the destabilizing force gradient for an X-point LCFS. (This has been checked, but it is not shown because the plot essentially duplicates Fig. 3.) The difference here is that the destabilizing force gradient includes a contribution due to the reaction of the wall to the plasma wire (see Sec. III A 1) and that due to the external coils.

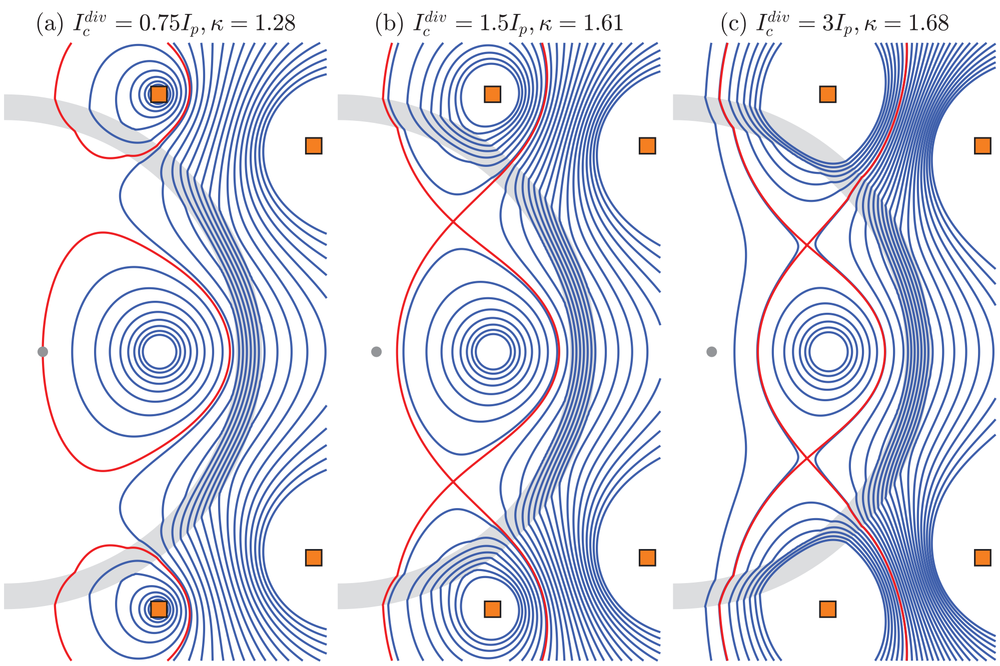

FIG. 10. Equilibrium poloidal magnetic flux surfaces for various divertor currents [(a) low, (b) intermediate, and (c) high]. The wall, shown in gray, has $r_i = 0.9 r_e$ and $\tilde{\mu} = 3$. Coils are plotted as orange squares; the vertical field coil current is adjusted in order to keep $R_p = 0.6 r_e$ constant. Red curves show the LCFS, defined either by the X-point or the inboard limiter at $R = 0.15 r_e$ (gray dot).

© Author(s) 2020

B. Time-dependent field

We now calculate the vector potential which satisfies (28) with the time derivative reinstated within the volume of the conducting ferromagnetic wall. As in Sec. II B, we let the plasma height grow as $z_p \propto e^{\gamma t}$ and calculate the induced currents in the wall, and then the corresponding back-reaction upon the plasma wire. The linearized perturbation to the vector potential has a general series solution of the form

$$a(r,\theta,t) = \sum_{\substack{\ell=2\\ \ell\,\mathrm{even}}}^{\infty} \hat{a}_\ell(r) e^{\gamma t} P_\ell^1(\cos\theta) \tag{44}$$

(cf. 17), where

$$\hat{a}_\ell e^{\gamma t} = \begin{cases} c_\ell^{(i)} \dfrac{r_i^{\ell+1} r_<^\ell}{R_p^\ell r_>^{\ell+1}} + d_\ell^{(i)} \left(\dfrac{r}{r_i}\right)^\ell, & (i) \\ c_\ell^{(w)} \mathsf{i}_\ell(y) + d_\ell^{(w)} \mathsf{k}_\ell(y), & (w) \\ c_\ell^{(e)} \left(\dfrac{r_i}{r}\right)^{\ell+1} & (e) \end{cases} \tag{45}$$

(cf. 18). Here, $\mathsf{i}_\ell(y) = (\pi/2y)^{1/2} \mathsf{I}_{\ell+\frac{1}{2}}(y)$ and $\mathsf{k}_\ell(y) = (\pi/2y)^{1/2} \mathsf{K}_{\ell+\frac{1}{2}}(y)$ are modified spherical Bessel functions and $r_\lessgtr$ is the lesser/greater of r and R_p. By comparison with a Taylor expansion of the plasma wire solution (29) about $z_p = 0$, it can be seen that

$$c_\ell^{(i)} = \frac{\mu_0 I_p z_p}{2} \frac{R_p^\ell}{r_i^{\ell+1}} P_\ell^0(0), \tag{46}$$

whereas the remaining coefficients are derived through application of the boundary conditions (27) at the interior-wall and wall-exterior interfaces (see Appendix C 3). Most importantly, the resulting horizontal magnetic flux density at the plasma location is, to leading order in z_p,

$$b_R = \sum_{\substack{\ell=2\\ \ell\,\mathrm{even}}}^{\infty} -\frac{\mu_0 I_p z_p}{2R_p^2} \ell(\ell+1) \frac{d_\ell^{(i)}}{c_\ell^{(i)}} \left(\frac{R_p}{r_i}\right)^{2\ell+1} \left[P_\ell^0(0)\right]^2 \tag{47}$$

(cf. 19), with $d_\ell^{(i)}/c_\ell^{(i)}$ given by (C20) and (C21). This expression gives the vertical Lorentz force acting on the displaced plasma wire due to the presence of the wall.

Having learnt in Sec. II that distinguishing between fast and slow (or thick- and thin-wall) instabilities proves a useful paradigm for understanding the ferromagnetic vertical stability problem, we adopt the same approach here. First taking the limit of a magnetically thick wall ($s \ll \delta_w$ or $\gamma\tau_{w0} \gg 1$), we have

$$\frac{d_\ell^{(i)}}{c_\ell^{(i)}} \approx -1 + \frac{(2\ell+1)\tilde{\mu}}{y_i} + \mathcal{O}\left(y_i^{-2}\right) \tag{48}$$

(cf. 20). Once again, this makes b_R a function of $\tilde{\mu}$ and γ only in the combination $\gamma/\tilde{\mu}$ since $y_i/\tilde{\mu} = r_i\sqrt{\mu_0\sigma\gamma/\tilde{\mu}}$, and hence (for a given plasma elongation), we can expect growth rates to grow by a factor $\tilde{\mu}$ when the wall may be considered magnetically thick. Note that taking just the leading-order term in (48) gives the maximum possible stabilizing wall force $b_{R,\max}$ (i.e., the ideal wall limit). Destabilizing force gradients which exceed this value will lead to unstable growth on the Alfvén time.

On the other hand, if the wall is magnetically thin, then the vertical force is the sum of the quasi-steady destabilizing ferromagnetic force (35) and a permeability-independent stabilizing term due to the induced wall currents,

$$\frac{d_\ell^{(i)}}{c_\ell^{(i)}} \approx \frac{D_\ell^{(p,i)}}{C_\ell^{(p,i)}} - \left(1 + \frac{2\ell+1}{\mu_0\sigma\gamma\delta_w r_w}\right)^{-1}. \tag{49}$$

See (C6) [or (C7) in the limit $\delta_w \ll r_w$] for $D_\ell^{(p,i)}/C_\ell^{(p,i)}$. The derivation of the second term very closely follows the equivalent cylindrical version (Appendix B).

C. Calculation of the growth rate

We are now in a position to calculate the vertical instability growth rate of a plasma wire within a conducting, ferromagnetic spherical shell, by solving the massless plasma force balance equation

$$b_R + z_p B_R' = 0 \tag{50}$$

(cf. 22), where for brevity we define

$$B_R' = \frac{\partial}{\partial z}\left(B_R^{(p)}\Big|_{z_p=0} + \sum_c B_R^{(c)} \right)_{\substack{R=R_p\\ z=0}} \tag{51}$$

as the total vertical force gradient due to the curvature of equilibrium field lines—see (34) and (41) for definitions of the plasma and coil contributions, respectively. The term in (50) associated with the time-dependent response of the wall, $b_R(\gamma)$, is given by (47).

Before we calculate any growth rates, it is worthwhile summarizing the forces that act on the plasma at the onset of a ferromagnetic VDE. These can be broken down into four contributions: two associated with the equilibrium field and two with the time-dependent field. They are as follows:

(1) The equilibrium curvature force due to external coil pairs, given by (41). This may be stabilizing or destabilizing, depending upon the exact arrangement of the coils, although for configurations where vertical stability is an issue will inevitably be destabilizing. Determined as a sum over any number of coil pairs, but because our model problem treats the plasma as a wire, only its point value is relevant.

(2) The equilibrium curvature force due to the response of the wall to the wire itself, given by (34), or see Fig. 8(b). This is always vertically stabilizing, but only because it reduces the plasma elongation. Although both this term and (1) are nominally functions of $\tilde{\mu}$, their sum (51) will be approximately fixed for a plasma of given elongation—the currents in the poloidal field coils will simply have to be adjusted in order to achieve it.

(3) The quasi-steady destabilizing ferromagnetic force (35), which is the force the wall would exert upon the plasma wire if it were held stationary at a small height z_p above the midplane. If the VDE occurs quickly relative to the resistive wall time ($\gamma\tau_{w0} \gg 1$), then the internal field does not have time to reconfigure to the ferromagnetic equilibrium of Sec. III A 1, and so this term does not contribute. On the other hand, for slow-growing instabilities ($\gamma\tau_{w0} \ll 1$), this term constitutes an

© Author(s) 2020

additional destabilizing influence which is independent of the plasma elongation.

(4) The force due to currents induced in the conducting wall, given by (47) with the contribution from (3) subtracted out. This term is always stabilizing but has a character which depends upon the instability growth rate. If it is fast, this contribution becomes (48), which is a function of $\gamma/\tilde{\mu}$ only. For slow growth, however, the induced currents are approximately independent of the magnetic permeability and given by the second term in (49).

In summary, (1) and (2) act independently of the growth rate and are tied to the plasma elongation. For $\gamma\tau_{w0} \gg 1$, (3) is negligible, whereas (4) is modified by $\gamma \to \gamma/\tilde{\mu}$ for non-unity $\tilde{\mu}$. For $\gamma\tau_{w0} \ll 1$, (3) provides an additional destabilizing ferromagnetic force, but (4) is unchanged by the existence of ferromagnetism. In either case, although the reasons for it are subtly different, the growth rate is expected to increase with $\tilde{\mu}$.

Figure 11 shows the calculated growth rate as a function of the destabilizing force and is the analogue of Fig. 5 in the cylindrical model problem—once again, the curves coalesce for $\gamma\tau_{w0} \gg 1$ in the thick-wall limit (a) and $\gamma\tau_{w0} \ll 1$ in the thin-wall limit (b). In the latter case, it is possible to derive an approximate expression for the growth rate by using the thin-wall limits (35) and (49) in the massless force balance (50) to obtain, for $\delta_w \ll s \ll r_w$,

$$\gamma\tau_{w0} \approx \frac{\delta_w}{r_w}\left[\left(2\frac{\delta_w}{r_w}\Delta_\mu - \frac{20}{3}\frac{B'_R r_i^5}{\mu_0 I_p R_p^3}\right)^{-1} - \frac{1}{5}\right]^{-1} \tag{52}$$

(cf. 24)—see (37) for Δ_μ. If the destabilizing force due to the equilibrium field line curvature B'_R is kept constant as $\tilde{\mu}$ varies, then the growth rate is given approximately by

$$\gamma\tau_{w0} \approx \gamma_0\tau_{w0} + 2\Delta_\mu\left(\frac{\delta_w}{r_w} + \frac{\gamma_0\tau_{w0}}{5}\right)^2 \tag{53}$$

(cf. 25). Plots of γ/γ_0 as a function of $\gamma_0\tau_{w0}$ using this formula show an agreement with the exact calculation and a functional dependence on γ_0, which is very similar to the cylindrical version of Fig. 6. Equation (53) for $\gamma_0\tau_{w0} \lesssim 1$ (and $\gamma = \tilde{\mu}\gamma_0$ for $\gamma_0\tau_{w0} \gtrsim 1$) therefore provides a convenient way to estimate the change in the instability growth rate accountable to ferromagnetic effects, for a spherical tokamak plasma of specified elongation κ and major radius R_p.

IV. DISCUSSION

We have explored the equilibrium and vertical stability characteristics of tokamaks with ferromagnetic walls through two related analytical models in cylindrical (Sec. II) and spherical (Sec. III) geometries. The former is more straightforward and so provides a useful handle on the problem, but we concentrate our discussion on the latter because of its richer physics content.

A. Equilibrium

From the study of radial force balance (Sec. III A 3), it is apparent that the presence of significant ferromagnetic material has a non-negligible effect upon the plasma equilibrium, with the mutual attraction between the two increasing demand on the vertical field coils in

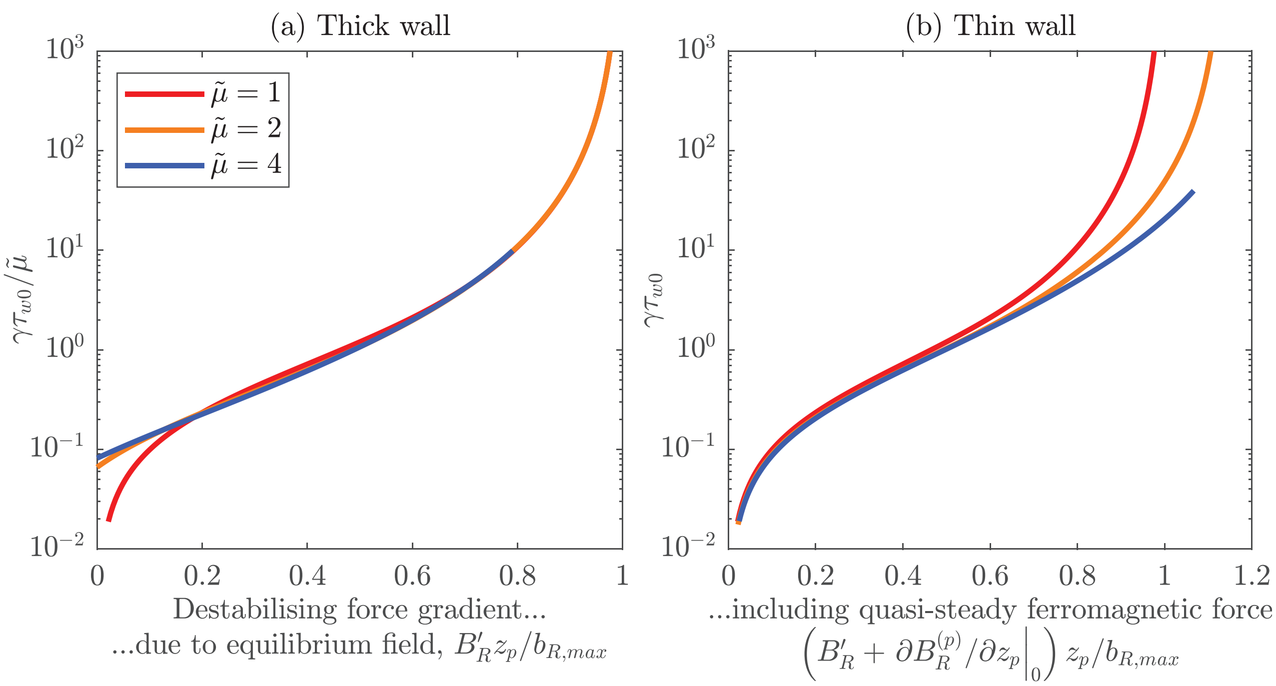

FIG. 11. Vertical instability growth rate as a function of the destabilizing force acting on the plasma, either (a) due to the equilibrium field line curvature [Eq. (51)] or (b) including the ferromagnetic force as well [right pane, Eq. (35)]. The former collapse in the limit of a thick wall, $\gamma\tau_{w0} \gg 1$ (note that the vertical axis is scaled by $\tilde{\mu}$), whereas the latter collapse for a thin wall, $\gamma\tau_{w0} \ll 1$. Geometry is as Fig. 10 with the divertor coil current I_c^{div} varying between 0 and $3.5I_p$, whereas the vertical field coil current is adjusted such that radial force balance (42) is maintained (cf. Fig. 5).

© Author(s) 2020

order to maintain radial force equilibrium (see Fig. 9 and previous experimental findings[20]). The effects are magnified the closer the plasma gets to the wall, to such a degree that radial equilibria with R_p above a certain critical value become unstable, at least in this model; for a distributed plasma current, the story may be different, but such an investigation lies beyond the present scope. Ferromagnetic effects also increase the divertor current necessary to obtain a certain elongation for a given plasma current and position because the wall's response to the plasma (Fig. 8, Sec. III A 1) acts to reduce elongation (i.e., is vertically stabilizing). For these two reasons at least, it is clear that ferromagnetic effects cannot be neglected in equilibrium calculations regarding tokamaks containing significant quantities of ferritic steel, and the above calculations should provide a useful first-order estimate of the required modifications to the applied external currents. Indeed, the present work could form the basis for a next-level equilibrium solver, which considers distributed plasma currents, multiple poloidal field coils, and additional passive conducting structures.

B. Vertical instability

The focus of our study has been on the modification to the vertical instability growth rate for a conducting wall with an effective relative magnetic permeability $\tilde{\mu} \sim 2-4$, as compared to the non-ferromagnetic case. Limits for fast and slow instabilities, similar to FRWMs,[11] have been established (Sec. III C, Fig. 11) to guide understanding of the physical mechanisms at play. Fast instabilities are skin-effect dominated, and the influence of ferromagnetism is to reduce penetration of magnetic flux into the wall, weakening its stabilizing response by a factor $\tilde{\mu}$ (again, this is analogous to FRWMs[16]). Slow instabilities allow time for the ferromagnetic response to the plasma's motion to rearrange itself such that it stays close to the equilibrium configuration of Sec. III A 1 and therefore provides an additional destabilizing force with a non-trivial dependence upon γ and $\tilde{\mu}$.

Whilst these limiting cases are useful for establishing intuition, a real tokamak is likely to operate in a regime where $\gamma\tau_{w0}$ is of order unity; smaller values correspond to meager plasma elongation and hence suboptimal performance, whereas pushing the elongation and therefore increasing the growth rate will make the plasma uncontrollable.[28] With this is mind, the full expression for the stabilizing wall force (see Sec. III B and Appendix C 3) should be used in order to estimate growth rates consistently [though note that the thin-wall approximation (52) works surprisingly well at intermediate $\gamma\tau_{w0}$, akin to Fig. 6]. The upshot is that changing the steel to ferromagnetic, while keeping everything else (geometry, plasma elongation, and electrical conductivity) constant results in an increase in the growth rate on the order of the effective magnetic permeability—see Fig. 6(b). This enhanced vertical instability must be accommodated by an improvement in the performance of active vertical control systems, even as ferromagnetic effects also erode their influence on the tokamak interior. The issue awaits a future detailed study, but it seems that special care must be taken in the design of vertical control systems for tokamaks containing ferritic steels.

1. Induced current distribution

The spatial structure of currents induced within the wall during a VDE will be of much interest when designing ferritic structural components for tokamaks; this is shown in Fig. 12 for the VDE onset of the same equilibria plotted in Fig. 10—recall that the magnetic permeability is $\tilde{\mu} = 3$ and the divertor coil current is varied with the plasma

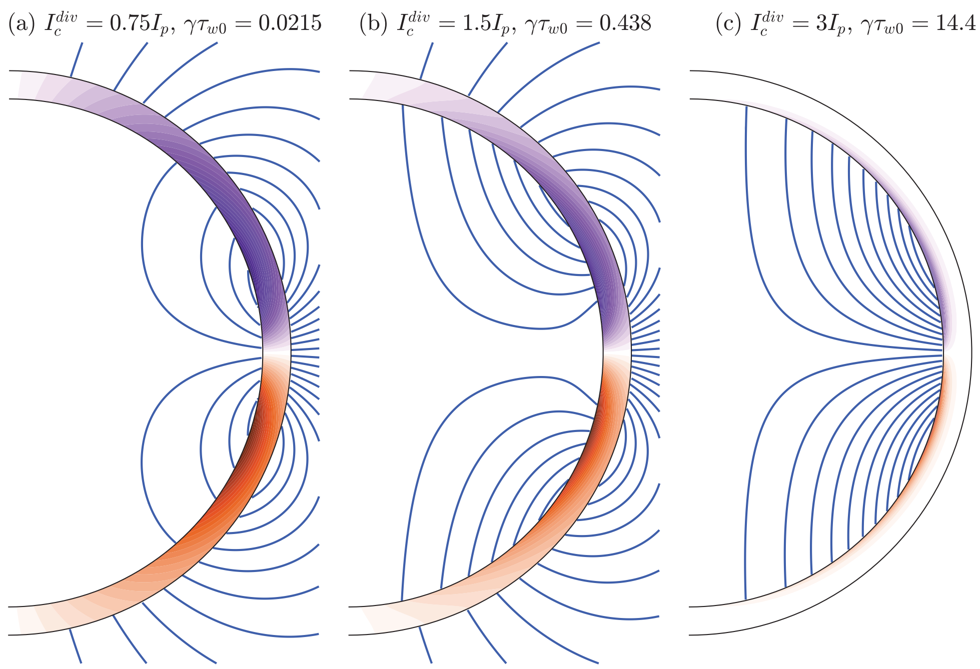

FIG. 12. Induced field at VDE onset for the equilibria of Fig. 10. Solid color shows the toroidal current density distribution within the conducting wall (orange positive and purple negative with respect to I_p) normalized to its maximum absolute value. Contour lines show poloidal magnetic flux surfaces in the vacuum regions associated with this current distribution. (a) A slow, (b) an intermediate, and (c) a fast instability.

© Author(s) 2020

major radius being held constant. A weak divertor current [Fig. 12(a)] implies a gentle destabilizing force gradient and therefore a slow-growing instability, such that $\gamma\tau_{w0} \ll 1$ and the currents within the wall occupy its entire thickness. On the other hand, if the divertor current is strong [Fig. 12(c)], then the growth rate is large ($\gamma\tau_{w0} \gg 1$) because the destabilizing force gradient is more severe. The perturbed current density is confined to a narrow skin of thickness $s \ll \delta_w$, and the associated magnetic flux is almost completely interior. An intermediate—probably most reactor-relevant—case with $\gamma\tau_{w0} \sim 1$ is shown in Fig. 12(b).

Observe that the induced current density is generally found in the outboard region of the wall, relatively close to the midplane. Recall that, in this model problem, our choice of a constant effective magnetic permeability $\tilde{\mu}$ neglects its true dependency on the toroidal magnetic flux [see (1)], which itself varies as $1/R$. However, since the induced currents are biased toward the outboard midplane, it seems reasonable to use the effective permeability there (at $R = r_i$, say) for the entire wall, at least as a first approximation. Furthermore, this suggests that there should not be any substantial modification to these results when the wall is not a full spherical shell but rather has coverage only on a limited portion of the outboard side, as for existing tritium breeding region designs.[18,29] We may add the caveats, however, that a distributed plasma might induce wall currents further from the midplane and that toroidally discrete wall elements may be different.[30]

C. Future work

The analytical models here naturally have limitations, which might be usefully addressed in future studies—as discussed above, the simplified wall geometries, constant (independent of R) $\tilde{\mu}$, single wire representation of the plasma current, and lack of any other passive conductors or control coils may all be cited as shortcomings, and one might add to this list the inflexibility due to enforced up-down symmetry or lack of non-linear evolution as studied in Ref. 12. Perhaps one of the most important inaccuracies is the choice of a toroidally continuous wall since tritium breeding is likely to be done in modules with ferritic structural elements that do not necessary link all the way around the torus. The induced currents in three-dimensional passive conductors[30,31] are very different to those in toroidally continuous ones, but one might expect the destabilizing quasi-steady ferromagnetic force to be broadly unchanged for discrete vs continuous components. The question remains open, but Ref. 16 discusses the effects of tiling ferromagnetic material and Ref. 32 proposes a route toward the numerical modeling of 3D ferromagnetic structures.

ACKNOWLEDGMENTS

OB was funded by a UKAEA-PPPL postdoctoral fellowship. This work received funding from the UK Department for Business, Energy and Industrial Strategy, and EPSRC under Grant No. EP/T012250/1.

APPENDIX A: APPLICATION OF BOUNDARY CONDITIONS IN THE CYLINDRICAL MODEL PROBLEM

1. Plasma wire

The boundary conditions at the wall-exterior interface r_e are as follows:

$$\text{Normal flux}: \ C_m^{(p,e)} = C_m^{(p,w)} + D_m^{(p,w)}(r_e/r_i)^{2m}, \tag{A1}$$

$$\text{Tangential field}: \ \tilde{\mu}C_m^{(p,e)} = C_m^{(p,w)} - D_m^{(p,w)}(r_e/r_i)^{2m}. \tag{A2}$$

Eliminating $C_m^{(p,e)}$, we get

$$(\tilde{\mu}-1)(r_i/r_e)^m C_m^{(p,w)} + (\tilde{\mu}+1)(r_e/r_i)^m D_m^{(p,w)} = 0. \tag{A3}$$

The boundary conditions at the interior-wall interface r_i are as follows:

$$\text{Normal flux}: \ C_m^{(p,w)} + D_m^{(p,w)} - D_m^{(p,i)} = C_m^{(p,i)}, \tag{A4}$$

$$\text{Tangential field}: \ C_m^{(p,w)} - D_m^{(p,w)} + \tilde{\mu}D_m^{(p,i)} = \tilde{\mu}C_m^{(p,i)}. \tag{A5}$$

Equations (A3)–(A5) may be solved simultaneously, with $C_m^{(p,e)}$ then coming from (A1),

$$\begin{pmatrix} D_m^{(p,i)} \\ C_m^{(p,w)} \\ D_m^{(p,w)} \\ C_m^{(p,e)} \end{pmatrix} = \left[\frac{\tilde{\mu}-1}{\tilde{\mu}+1}\left(\frac{r_i}{r_e}\right)^m - \frac{\tilde{\mu}+1}{\tilde{\mu}-1}\left(\frac{r_e}{r_i}\right)^m\right]^{-1} \times \begin{pmatrix} (r_i/r_e)^m - (r_e/r_i)^m \\ -2\tilde{\mu}(r_e/r_i)^m/(\tilde{\mu}-1) \\ 2\tilde{\mu}(r_i/r_e)^m/(\tilde{\mu}+1) \\ -4\tilde{\mu}(r_e/r_i)^m/(\tilde{\mu}^2-1) \end{pmatrix} C_m^{(p,i)}. \tag{A6}$$

2. Divertor coils

The boundary conditions at the interior-wall interface r_i are as follows:

$$\text{Normal flux}: \ D_m^{(c,i)} = C_m^{(c,w)} + D_m^{(c,w)}, \tag{A7}$$

$$\text{Tangential field}: \ \tilde{\mu}D_m^{(c,i)} = -C_m^{(c,w)} + D_m^{(c,w)}. \tag{A8}$$

Eliminating $D_m^{(c,i)}$, we get

$$(\tilde{\mu}+1)C_m^{(c,w)} + (\tilde{\mu}-1)D_m^{(c,w)} = 0. \tag{A9}$$

The boundary conditions at the wall-exterior interface r_e are as follows:

Normal flux:

$$C_m^{(c,w)} + D_m^{(c,w)}(r_e/r_i)^{2m} - C_m^{(c,e)} = D_m^{(c,e)}(r_e/r_i)^{2m}. \tag{A10}$$

Tangential field:

$$-C_m^{(c,w)} + D_m^{(c,w)}(r_e/r_i)^{2m} + \tilde{\mu}C_m^{(c,e)} = \tilde{\mu}D_m^{(c,e)}(r_e/r_i)^{2m}. \tag{A11}$$

Equations (A9)–(A11) may be solved simultaneously, with $D_m^{(c,i)}$ then coming from (A7),

$$\begin{pmatrix} D_m^{(c,i)} \\ C_m^{(c,w)} \\ D_m^{(c,w)} \\ C_m^{(c,e)} \end{pmatrix} = \left[\frac{\tilde{\mu}-1}{\tilde{\mu}+1}\left(\frac{r_i}{r_e}\right)^m - \frac{\tilde{\mu}+1}{\tilde{\mu}-1}\left(\frac{r_e}{r_i}\right)^m\right]^{-1} \times \begin{pmatrix} -4\tilde{\mu}(r_i/r_e)^m/(\tilde{\mu}^2-1) \\ 2\tilde{\mu}(r_i/r_e)^m/(\tilde{\mu}+1) \\ -2\tilde{\mu}(r_i/r_e)^m/(\tilde{\mu}-1) \\ (r_i/r_e)^m - (r_e/r_i)^m \end{pmatrix} (r_e/r_i)^{2m} D_m^{(c,e)}. \tag{A12}$$

© Author(s) 2020

3. Time-dependent field

The boundary conditions at the wall-exterior interface r_e are as follows:

Normal flux:

$$(r_i/r_e)c^{(e)} = \mathsf{I}_1(y_e)c^{(w)} + \mathsf{K}_1(y_e)d^{(w)}. \tag{A13}$$

Tangential field:

$$\tilde{\mu}(r_i/r_e)c^{(e)} = [-y_e\mathsf{I}_0(y_e) + \mathsf{I}_1(y_e)]c^{(w)} + [y_e\mathsf{K}_0(y_e) + \mathsf{K}_1(y_e)]d^{(w)}. \tag{A14}$$

Eliminating $c^{(e)}$, we get

$$\begin{aligned}&[y_e\mathsf{I}_0(y_e) + (\tilde{\mu}-1)\mathsf{I}_1(y_e)]c^{(w)}\\ &\quad+[-y_e\mathsf{K}_0(y_e) + (\tilde{\mu}-1)\mathsf{K}_1(y_e)]d^{(w)} = 0.\end{aligned} \tag{A15}$$

The boundary conditions at the interior-wall interface r_i are as follows:

Normal flux:

$$\mathsf{I}_1(y_i)c^{(w)} + \mathsf{K}_1(y_i)d^{(w)} - d^{(i)} = c^{(i)}. \tag{A16}$$

Tangential field:

$$-y_i\mathsf{I}_0(y_i)c^{(w)} + y_i\mathsf{K}_0(y_i)d^{(w)} + (\tilde{\mu}+1)d^{(i)} = (\tilde{\mu}-1)c^{(i)}. \tag{A17}$$

Equations (A15)–(A17) may be solved simultaneously for the coefficients $d^{(i)}$, $c^{(w)}$, and $d^{(w)}$, with $c^{(e)}$ then coming from (A13); in particular, the internal coefficients are related by

$$\frac{d^{(i)}}{c^{(i)}} = \frac{\alpha_\mathsf{I}^+ - \alpha_\mathsf{K}^+}{\alpha_\mathsf{I}^- - \alpha_\mathsf{K}^-}, \quad \text{where} \quad \alpha_\mathsf{I}^\pm = \frac{\pm y_i\mathsf{I}_0(y_i) + (\tilde{\mu}\mp 1)\mathsf{I}_1(y_i)}{y_e\mathsf{I}_0(y_e) + (\tilde{\mu}-1)\mathsf{I}_1(y_e)}, \tag{A18}$$

and $\alpha_\mathsf{K}^\pm$ is the same expression with $\mathsf{I}_0 \to -\mathsf{K}_0$ and $\mathsf{I}_1 \to \mathsf{K}_1$, with $y_{i,e} = r_{i,e}\sqrt{\mu_1\sigma\gamma}$.

APPENDIX B: THIN-WALL LIMIT OF THE CYLINDRICAL PROBLEM: STABILIZING FORCE

Within the wall itself, the flux function $\psi^{(w)}$ satisfies (4), and hence, solutions of the form (17) obey the differential equation as follows:

$$\frac{\mathrm{d}}{\mathrm{d}r}\left(r\frac{\mathrm{d}\hat{\psi}^{(w)}}{\mathrm{d}r}\right) = \left(\mu_1\sigma\gamma r + \frac{1}{r}\right)\hat{\psi}^{(w)}. \tag{B1}$$

We now integrate this over the thickness of the wall, from $r = r_i = r_w - \delta_w/2$ to $r = r_e = r_w + \delta_w/2$. Assuming that the wall is thin, such that the right-hand side of (B1) is approximately constant across it and terms of order δ_w/r_w may be ignored, this becomes

$$\left\langle\frac{\mathrm{d}\hat{\psi}^{(w)}}{\mathrm{d}r}\right\rangle \approx \frac{\delta_w}{r_w^2}(\mu_1\sigma\gamma r_w^2 + 1)\hat{\psi}^{(w)}(r_w), \tag{B2}$$

where the angled brackets represent the jump across the wall. This quantity is related to the vacuum solutions by the boundary conditions (6). Furthermore, the right-hand side of (B2) simplifies if the skin depth is much less than the wall radius (such that $\delta_w \ll s \ll r_w$). Then, we have

$$\left\langle\frac{\mathrm{d}\hat{\psi}}{\mathrm{d}r}\right\rangle \approx \mu_0\sigma\gamma\delta_w\hat{\psi}(r_w), \tag{B3}$$

where it is now understood that $\hat{\psi}$ pertains to the vacuum flux function ($\hat{\psi}^{(i)}$ and $\hat{\psi}^{(e)}$) and the wall thickness has been taken to zero. Note how this expression is independent of the magnetic permeability of the wall. Using the vacuum solution of the form (18), the corresponding matching equation is

$$c^{(i)} - d^{(i)} \approx (\mu_0\sigma\gamma\delta_w r_w + 1)c^{(e)}, \tag{B4}$$

and since the continuity of flux for a thin wall demands $c^{(i)} + d^{(i)} \approx c^{(e)}$, the approximate solution has

$$d^{(i)} \approx -\left(1 + \frac{2}{\mu_0\sigma\gamma\delta_w r_w}\right)^{-1} c^{(i)}. \tag{B5}$$

APPENDIX C: APPLICATION OF BOUNDARY CONDITIONS IN THE SPHERICAL MODEL PROBLEM

1. Plasma wire

The boundary conditions at the wall-exterior interface r_e are as follows:

Normal flux:

$$C_\ell^{(p,e)} = C_\ell^{(p,w)} + (r_e/r_i)^{2\ell+1}D_\ell^{(p,w)}. \tag{C1}$$

Tangential field:

$$\tilde{\mu}\ell C_\ell^{(p,e)} = \ell C_\ell^{(p,w)} - (\ell+1)(r_e/r_i)^{2\ell+1}D_\ell^{(p,w)}. \tag{C2}$$

Eliminating $C_\ell^{(p,e)}$, we get

$$(\tilde{\mu}-1)\ell C_\ell^{(p,w)} + (\tilde{\mu}\ell + \ell + 1)(r_e/r_i)^{2\ell+1}D_\ell^{(p,w)} = 0. \tag{C3}$$

The boundary conditions at the interior-wall interface r_i are as follows:

Normal flux:

$$C_\ell^{(p,w)} + D_\ell^{(p,w)} - D_\ell^{(p,i)} = C_\ell^{(p,i)}. \tag{C4}$$

Tangential field:

$$\ell C_\ell^{(p,w)} - (\ell+1)D_\ell^{(p,w)} + \tilde{\mu}(\ell+1)D_\ell^{(p,i)} = \tilde{\mu}\ell C_\ell^{(p,i)}. \tag{C5}$$

Equations (C3)–(C5) may be solved simultaneously, with $C_\ell^{(p,e)}$ then coming from (C1). In particular, the internal coefficients are related by

$$\frac{D_\ell^{(p,i)}}{C_\ell^{(p,i)}} = \frac{1-(r_e/r_i)^{2\ell+1}}{\dfrac{(\tilde{\mu}-1)(\ell+1)}{\tilde{\mu}\ell+\ell+1} - \dfrac{\tilde{\mu}\ell+\ell+\tilde{\mu}}{\ell(\tilde{\mu}-1)}(r_e/r_i)^{2\ell+1}}. \tag{C6}$$

If the wall is geometrically thin, $\delta_w \ll r_i$, then

$$\frac{D_\ell^{(p,i)}}{C_\ell^{(p,i)}} \approx \frac{\ell(\tilde{\mu}-1)(\tilde{\mu}\ell+\ell+1)}{(2\ell+1)\tilde{\mu}}\frac{\delta_w}{r_i}. \tag{C7}$$

© Author(s) 2020

2. External coil pair

The boundary conditions at the interior-wall interface r_i are as follows:

Normal flux:

$$D_\ell^{(c,i)} = C_\ell^{(c,w)} + D_\ell^{(c,w)}. \tag{C8}$$

Tangential field:

$$\tilde{\mu}(\ell+1)D_\ell^{(c,i)} = -\ell C_\ell^{(c,w)} + (\ell+1)D_\ell^{(c,w)}. \tag{C9}$$

Eliminating $D_\ell^{(c,i)}$, we get

$$(\tilde{\mu}\ell + \ell + \tilde{\mu})C_\ell^{(c,w)} + (\tilde{\mu}-1)(\ell+1)D_\ell^{(c,w)} = 0. \tag{C10}$$

The boundary conditions at the wall-exterior interface r_e are as follows:

Normal flux:

$$C_\ell^{(c,w)} + (r_e/r_i)^{2\ell+1}D_\ell^{(c,w)} - C_\ell^{(c,e)} = (r_e/r_i)^{2\ell+1}D_\ell^{(c,e)}. \tag{C11}$$

Tangential field:

$$\begin{aligned}&-\ell C_\ell^{(c,w)} + (\ell+1)(r_e/r_i)^{2\ell+1}D_\ell^{(c,w)} + \tilde{\mu}\ell C_\ell^{(c,e)}\\ &\quad = \tilde{\mu}(\ell+1)(r_e/r_i)^{2\ell+1}D_\ell^{(c,e)}.\end{aligned} \tag{C12}$$

Equations (C10)–(C12) may be solved simultaneously, with $D_\ell^{(c,i)}$ then coming from (C8); these internal coefficients are given explicitly by

$$\frac{D_\ell^{(c,i)}}{D_\ell^{(c,e)}} = \frac{\tilde{\mu}(2\ell+1)^2(r_e/r_i)^{2\ell+1}}{\left[\begin{matrix}(\tilde{\mu}\ell+\ell+\tilde{\mu})(\tilde{\mu}\ell+\ell+1)(r_e/r_i)^{2\ell+1}\\ -\ell(\ell+1)(\tilde{\mu}-1)^2\end{matrix}\right]}. \tag{C13}$$

If the wall is geometrically thin, $\delta_w \ll r_i$, then

$$\frac{D_\ell^{(c,i)}}{D_\ell^{(c,e)}} \approx 1 - \frac{\ell(\ell+1)(\tilde{\mu}-1)^2}{(2\ell+1)\tilde{\mu}}\frac{\delta_w}{r_i}. \tag{C14}$$

3. Time-dependent field

The boundary conditions at the wall-exterior interface r_e are as follows:

Normal flux:

$$(r_i/r_e)^{\ell+1}c_\ell^{(e)} = \mathsf{i}_\ell(y_e)c_\ell^{(w)} + \mathsf{k}_\ell(y_e)d_\ell^{(w)}. \tag{C15}$$

Tangential field:

$$\begin{aligned}\ell\tilde{\mu}(r_i/r_e)^{\ell+1}c_\ell^{(e)} &= [\ell\mathsf{i}_\ell(y_e) - y_e\mathsf{i}_{\ell-1}(y_e)]c_\ell^{(w)}\\ &\quad + [\ell\mathsf{k}_\ell(y_e) + y_e\mathsf{k}_{\ell-1}(y_e)]d_\ell^{(w)}.\end{aligned} \tag{C16}$$

Eliminating $c_\ell^{(e)}$, we get

$$\begin{aligned}&[\ell(\tilde{\mu}-1)\mathsf{i}_\ell(y_e) + y_e\mathsf{i}_{\ell-1}(y_e)]c_\ell^{(w)}\\ &\quad + [\ell(\tilde{\mu}-1)\mathsf{k}_\ell(y_e) - y_e\mathsf{k}_{\ell-1}(y_e)]d_\ell^{(w)} = 0.\end{aligned} \tag{C17}$$

The boundary conditions at the interior-wall interface r_i are as follows:

Normal flux:

$$\mathsf{i}_\ell(y_i)c_\ell^{(w)} + \mathsf{k}_\ell(y_i)d_\ell^{(w)} - d_\ell^{(i)} = c_\ell^{(i)}. \tag{C18}$$

Tangential field:

$$-y_i\mathsf{i}_{\ell-1}(y_i)c_\ell^{(w)} + y_i\mathsf{k}_{\ell-1}(y_i)d_\ell^{(w)} + (\tilde{\mu}\ell + \ell + \tilde{\mu})d_\ell^{(i)} = \ell(\tilde{\mu}-1)c_\ell^{(i)}. \tag{C19}$$

Equations (C17)–(C19) may be solved simultaneously for the coefficients $d_\ell^{(i)}$, $c_\ell^{(w)}$, and $d_\ell^{(w)}$, with $c_\ell^{(e)}$ then coming from (C15); in particular, the internal coefficients are given by

$$\frac{d_\ell^{(i)}}{c_\ell^{(i)}} = -\frac{\alpha_\mathsf{i}^+ - \alpha_\mathsf{k}^+}{\alpha_\mathsf{i}^- - \alpha_\mathsf{k}^-}, \tag{C20}$$

where

$$\alpha_\mathsf{i}^\pm = \frac{\left[\tilde{\mu}\left(\pm\ell\pm\frac{1}{2}-\frac{1}{2}\right)-\ell\right]\mathsf{i}_\ell(y_i) + y_i\mathsf{i}_{\ell-1}(y_i)}{\ell(\tilde{\mu}-1)\mathsf{i}_\ell(y_e) + y_e\mathsf{i}_{\ell-1}(y_e)} \tag{C21}$$

and $\alpha_\mathsf{k}^\pm$ is the same expression with $\mathsf{i}_\ell \to \mathsf{k}_\ell$ and $\mathsf{i}_{\ell-1} \to -\mathsf{k}_{\ell-1}$.

DATA AVAILABILITY

Data sharing is not applicable to this article as no new data were created or analyzed in this study.

REFERENCES

[1] S. J. Zinkle, "Fusion materials science: Overview of challenges and recent progress," Phys. Plasmas **12**, 058101 (2005).

[2] A. Kohyama, A. Hishinuma, D. S. Gelles, R. L. Klueh, W. Dietz, and K. Ehrlich, "Low-activation ferritic and martensitic steels for fusion application," J. Nucl. Mater. **233–237**, 138–147 (1996).

[3] A. Kohyama, A. Hishinuma, Y. Kohno, K. Shiba, and A. Sagara, "The development of ferritic steels for DEMO blanket," Fusion Eng. Des. **41**, 1–6 (1998).

[4] K. Mergia and N. Boukos, "Structural, thermal, electrical and magnetic properties of Eurofer 97 steel," J. Nucl. Mater. **373**, 1–8 (2008).

[5] K. Ioki, V. Barabash, A. Cardella, F. Elio, Y. Gohar, G. Janeschitz, G. Johnson, G. Kalinin, D. Lousteau, M. Onozuka, R. Parker, G. Sannazzaro, and R. Tivey, "Design and material selection for ITER first wall/blanket, divertor and vacuum vessel," J. Nucl. Mater. **258–263**, 74–84 (1998).

[6] A. Portone, M. Roccella, R. Roccella, F. Lucca, and G. Ramogida, "The ITER TF coil ripple: Evaluation of ripple attenuation using Fe insert and of ripple enhancement produced by TBM," in Proceedings of the Eight International Symposium on Fusion Nuclear Technology [Fusion Eng. Des. **83**, 1619–1624 (2008)].

[7] D. A. Gates, J. Menard, R. Maingi, S. Kaye, S. A. Sabbagh, S. Diem, J. R. Wilson, M. G. Bell, R. E. Bell, J. Ferron, E. D. Fredrickson, C. E. Kessel, B. P. LeBlanc, F. Levinton, J. Manickam, D. Mueller, R. Raman, T. Stevenson, D. Stutman, G. Taylor, K. Tritz, and H. Yu, "Progress towards steady state at low aspect ratio on the National Spherical Torus Experiment (NSTX)," Nucl. Fusion **47**, 1376–1382 (2007).

[8] D. Brunner, A. Q. Kuang, B. LaBombard, and J. L. Terry, "The dependence of divertor power sharing on magnetic flux balance in near double-null configurations on Alcator C-Mod," Nucl. Fusion **58**, 076010 (2018).

[9] C. Bachmann, W. Biel, S. Ciattaglia, G. Federici, F. Maviglia, G. Mazzone, G. Ramogida, F. Villone, and N. Taylor, "Initial definition of structural load conditions in DEMO," in Proceedings of the 29th Symposium of Fusion Technology (SOFT-29), Prague, Czech Republic, 5–9 September 2016 [Fusion Eng. Des. **124**, 633–637 (2017)].

[10] J. D. Jackson, *Classical Electrodynamics*, 3rd ed. (Wiley, New York, 1999).

© Author(s) 2020

[11]V. D. Pustovitov and V. V. Yanovskiy, "Ferromagnetic effects in the theory of slow and fast resistive wall modes in tokamaks," Phys. Plasmas **21**, 022516 (2014).
[12]D. Pfefferlé and A. Bhattacharjee, "Algebraic motion of vertically displacing plasmas," Phys. Plasmas **25**, 022516 (2018).
[13]V. S. Mukhovatov and V. D. Shafranov, "Plasma equilibrium in a tokamak," Nucl. Fusion **11**, 605–633 (1971).
[14]E. A. Lazarus, J. B. Lister, and G. H. Neilson, "Control of the vertical instability in tokamaks," Nucl. Fusion **30**, 111–141 (1990).
[15]J. P. Levesque, P. E. Hughes, J. Bialek, P. J. Byrne, M. E. Mauel, G. A. Navratil, Q. Peng, D. J. Rhodes, and C. C. Stoafer, "Active and passive kink mode studies in a tokamak with a movable ferromagnetic wall," Phys. Plasmas **22**, 056102 (2015).
[16]P. E. Hughes, J. P. Levesque, and G. A. Navratil, "Dynamics of MHD instabilities near a ferromagnetic wall," Nucl. Fusion **58**, 126009 (2018).
[17]A. Kirk, G. F. Counsell, H. R. Wilson, J.-W. Ahn, R. Akers, E. R. Arends, J. Dowling, R. Martin, H. Meyer, M. Hole, M. Price, P. B. Snyder, D. Taylor, M. J. Walsh, Y. Yang, and t. M. team, "ELM characteristics in MAST," Plasma Phys. Controlled Fusion **46**, 551–572 (2004).
[18]J. E. Menard, T. Brown, L. El-Guebaly, M. Boyer, J. Canik, B. Colling, R. Raman, Z. Wang, Y. Zhai, P. Buxton, B. Covele, C. D'Angelo, A. Davis, S. Gerhardt, M. Gryaznevich, M. Harb, T. C. Hender, S. Kaye, D. Kingham, M. Kotschenreuther, S. Mahajan, R. Maingi, E. Marriott, E. T. Meier, L. Mynsberge, C. Neumeyer, M. Ono, J.-K. Park, S. A. Sabbagh, V. Soukhanovskii, P. Valanju, and R. Woolley, "Fusion nuclear science facilities and pilot plants based on the spherical tokamak," Nucl. Fusion **56**, 106023 (2016).
[19]D. I. Kiramov and B. N. Breizman, "Model of vertical plasma motion during the current quench," Phys. Plasmas **24**, 100702 (2017).
[20]K. Tsuzuki, H. Kimura, H. Kawashima, M. Sato, K. Kamiya, K. Shinohara, H. Ogawa, K. Hoshino, M. Bakhtiari, S. Kasai, K. Uehara, H. Sasao, Y. Kusama, N. Isei, Y. Miura, T. Ogawa, M. Yamamoto, T. Shibata, K. Kikuchi, K. Miyachi, T. Ito, H. Ajikawa, S. Nomura, H. Tsutsui, R. Shimada, T. Ido, Y. Hamada, N. Fukumoto, M. Nagata, T. Uyama, H. Niimi, S. Yatsu, N. Kayukawa, T. Hino, Y. Hirohata, Y. Nagashima, A. Ejiri, A. Amemiya, Y. Sadamoto, and A. Tsushima, "High performance tokamak experiments with a ferritic steel wall on JFT-2M," Nucl. Fusion **43**, 1288–1293 (2003).
[21]M. Mori, N. Suzuki, T. Shoji, I. Yanagisawa, T. Tani, and Y. Matsuzaki, "Stability limit of feedback control of vertical plasma position in the JFT-2M tokamak," Nucl. Fusion **27**, 725–734 (1987).
[22]J. Wesson, *Tokamaks*, 4th ed. (Oxford University Press, Oxford, 2011).
[23]M. P. Gryaznevich, T. G. Kilovataya, and V. N. Pyatov, "Effect of a ferromagnet on the equilibrium of a tokamak plasma," Sov. J. Plasma Phys. **9**, 414–417 (1983).
[24]E. R. Solano, G. H. Neilson, and L. L. Lao, "Equilibrium and stability studies for an iron core tokamak with a poloidal divertor," Nucl. Fusion **30**, 1107–1115 (1990).
[25]D. P. O'Brien, L. L. Lao, E. R. Solano, M. Garribba, T. S. Taylor, J. G. Cordey, and J. J. Ellis, "Equilibrium analysis of iron core tokamaks using a full domain method," Nucl. Fusion **32**, 1351–1360 (1992).
[26]W. Zwingmann, "Equilibrium analysis of steady state tokamak discharges," Nucl. Fusion **43**, 842–850 (2003).
[27]L. C. Appel and I. Lupelli, "Equilibrium reconstruction in an iron core tokamak using a deterministic magnetisation model," Comput. Phys. Commun. **223**, 1–17 (2018).
[28]J. A. Leuer, "Passive vertical stability in the next generation tokamaks," Fusion Technol. **15**, 489–494 (1989).
[29]D.-K. Sze, M. Tillack, and L. El-Guebaly, "Blanket system selection for the ARIES-ST," Fusion Eng. Des. **48**, 371–378 (2000).
[30]V. D. Pustovitov, "Disruption forces on the tokamak wall with and without poloidal currents," Plasma Phys. Controlled Fusion **59**, 055008 (2017).
[31]P. H. Titus, S. Avasaralla, A. Brooks, and R. Hatcher, "NSTX disruption simulations of detailed divertor and passive plate models by vector potential transfer from OPERA global analysis results," in Proceedings of the 26th Symposium of Fusion Technology (SOFT-26) [Fusion Eng. Des. **86**, 1784–1790 (2011)].
[32]L. Barbato, S. Mastrostefano, G. Rubinacci, S. Ventre, and F. Villone, "Effect of 3D ferromagnetic materials on plasma nonlinear evolution in fusion devices," in 42nd EPS Conference on Plasma Physics, Lisbon, 2015.

© Author(s) 2020